Geologic Inheritance and Earthquake Rupture Processes: The 1905 M ≥ 8 Tsetserleg-Bulnay Strike-Slip Earthquake Sequence, Mongolia

Jin-Hyuck Choi, Yann Klinger, Matthieu Ferry, J.F. Ritz, Robin Kurtz, Magali Rizza, Laurent Bollinger, Battogtokh Davaasambuu, Nyambayar Tsend-Ayush, Sodnomsambuu Demberel

AGU PUBLICATIONS

JGR

Journal of Geophysical Research: Solid Earth

RESEARCH ARTICLE
10.1002/2017JB013962

Key Points:
- Full 676 km long surface rupture of the 1905 Tsetserleg-Bulnay earthquake was mapped based on submetric optical satellite image and field observation
- Detailed rupture geometry and the most complete data set of horizontal offset (276 new measurements) was acquired along the 1905 earthquake ruptures
- Along-strike variations in rupture pattern, secondary ruptures, and coseismic offsets correlate with local geology and structural imprints

Supporting Information:
- Supporting Information S1
- Data Set S1

Correspondence to:
J.-H. Choi,
cjh9521@kigam.re.kr

Citation:
Choi, J.-H., Klinger, Y., Ferry, M., Ritz, J.-F., Kurtz, R., Rizza, M., … Demberel, S. (2018). Geologic inheritance and earthquake rupture processes: The 1905 M ≥ 8 Tsetserleg-Bulnay strike-slip earthquake sequence, Mongolia. *Journal of Geophysical Research: Solid Earth*, *123*, 1925–1953. https://doi.org/10.1002/2017JB013962

Received 9 JAN 2017
Accepted 22 JAN 2018
Accepted article online 25 JAN 2018
Published online 21 FEB 2018

Geologic Inheritance and Earthquake Rupture Processes: The 1905 M ≥ 8 Tsetserleg-Bulnay Strike-Slip Earthquake Sequence, Mongolia

Jin-Hyuck Choi[1,2], Yann Klinger[1], Matthieu Ferry[3], Jean-François Ritz[3], Robin Kurtz[3], Magali Rizza[4], Laurent Bollinger[5], Battogtokh Davaasambuu[3,6], Nyambayar Tsend-Ayush[6], and Sodnomsambuu Demberel[6]

[1]Institut de Physique du Globe de Paris - CNRS, Sorbonne Paris Cité, Université Paris Diderot, Paris, France, [2]Korea Institute of Geosciences and Mineral Resources, Daejeon, South Korea, [3]Géosciences Montpellier, Université de Montpellier, Montpellier, France, [4]Aix-Marseille Université, CNRS, IRD, CEREGE UM34, Aix-en-Provence, France, [5]CEA, DAM, Arpajon, France, [6]Institute of Astronomy and Geophysics, Ulaanbaatar, Mongolia

Abstract In 1905, 14 days apart, two M ~ 8 continental strike-slip earthquakes, the Tsetserleg and Bulnay earthquakes, occurred on the Bulnay fault system, in Mongolia. Together, they ruptured four individual faults, with a total length of ~676 km. Using submetric optical satellite images "Pleiades" with ground resolution of 0.5 m, complemented by field observation, we mapped in detail the entire surface rupture associated with this earthquake sequence. Surface rupture along the main Bulnay fault is ~388 km in length, striking nearly E-W. The rupture is formed by a series of fault segments that are 29 km long on average, separated by geometric discontinuities. Although there is a difference of about 2 m in the average slip between the western and eastern parts of the Bulnay rupture, along-fault slip variations are overall limited, resulting in a smooth slip distribution, except for local slip deficit at segment boundaries. We show that damage, including short branches and secondary faulting, associated with the rupture propagation, occurred significantly more often along the western part of the Bulnay rupture, while the eastern part of the rupture appears more localized and thus possibly structurally simpler. Eventually, the difference of slip between the western and eastern parts of the rupture is attributed to this difference of rupture localization, associated at first order with a lateral change in the local geology. Damage associated to rupture branching appears to be located asymmetrically along the extensional side of the strike-slip rupture and shows a strong dependence on structural geologic inheritance.

1. Introduction

Variability in rupture geometry and slip distribution appears more and more as key parameters to study interactions between geologic structures and earthquake rupture processes (e.g., King et al., 2005; King & Nabelek, 1985; Klinger, 2010; Sieh et al., 1993; Wesnousky, 2008). High-resolution rupture maps, involving an unprecedented level of detail for rupture geometries and lateral slip variations, have started to become available in the last decade due to progressive availability for civil researchers of submetric optical satellite images (e.g., Klinger et al., 2005; Xu et al., 2006). In parallel, new remote sensing methodologies have improved our capacity to measure horizontal and vertical displacements down to the actual rupture trace with a resolution of only few meters (Grandin et al., 2009; Klinger et al., 2006; Vallage et al., 2015, 2016). Eventually, these new data sets are starting to be introduced in numerical rupture models, although the current level of data complexity is still beyond standard modeling capacities (e.g., Duan & Oglesby, 2006; Finzi & Langer, 2012; Harris & Day, 1999; Hu et al., 2016; Lozos et al., 2011; Oglesby et al., 2008; Thomas et al., 2017). Earthquakes that were recently documented demonstrate that inherited fault geometries, such as fault bends, steps, branches, and their related segment geometry, can control the propagation and path of an earthquake rupture (Choi et al., 2012; Haeussler et al., 2004; Klinger et al., 2005; Lettis et al., 2002; Vallage et al., 2016; Wesnousky, 2008) and the rupture history over multiple seismic events (Klinger et al., 2011, 2017; Schwartz et al., 2012; Zielke et al., 2015). These results have been regarded as key parameters to assess potential for rupture of large earthquakes in given active fault systems, with significant implications for seismic hazard (Mignan et al., 2015).

In 1905 two large strike-slip earthquakes occurred on the Bulnay fault system, in the northwestern part of Mongolia (Figure 1). The magnitude M ~ 8 Tsetserleg earthquake occurred on 9 July at 9:40 a.m. universal time, and the M > 8 Bulnay earthquake occurred 14 days later, on 23 July at 2:46 a.m. universal time. These two

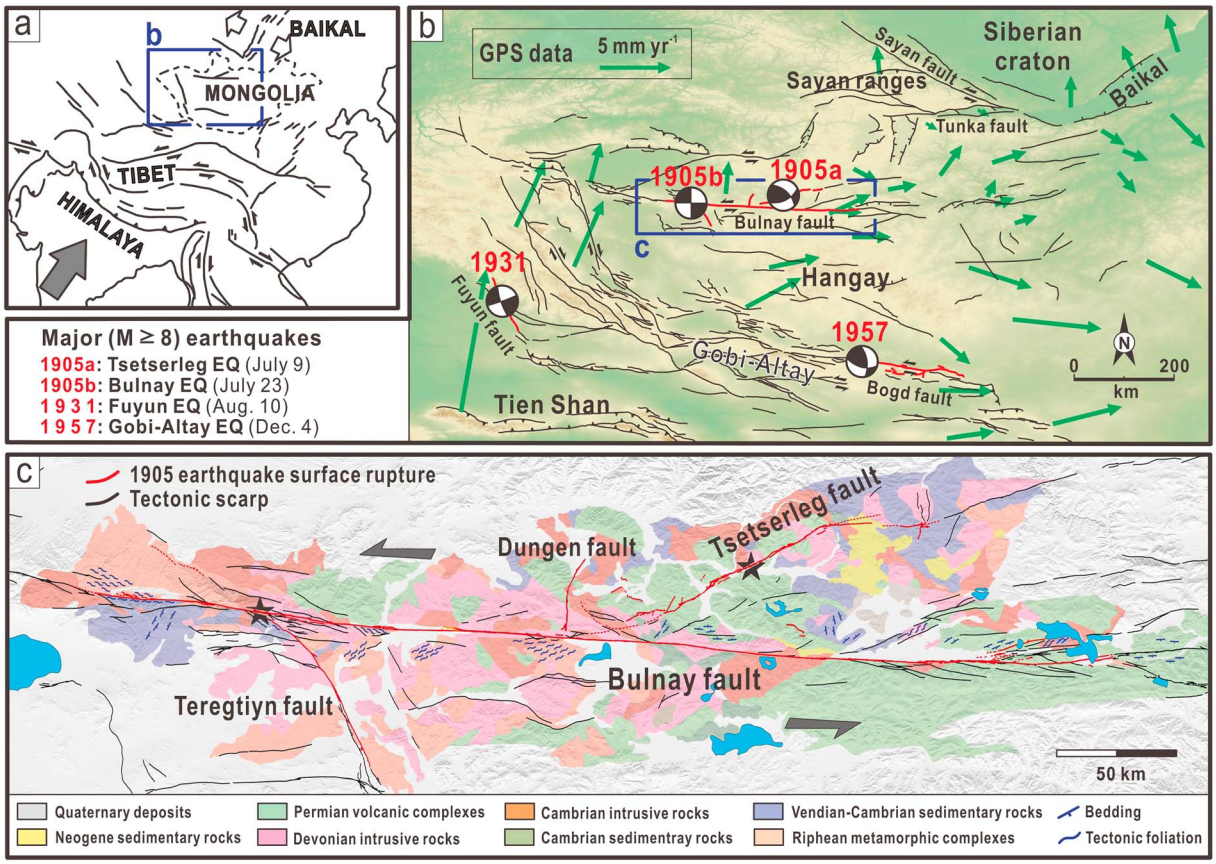

Figure 1. (a) Simplified tectonic map of study region. (b) Tectonic setting of western Mongolia. Surface ruptures associated with major (M ≥ 8) earthquakes during the last century are in red. Fault plane solutions constrained by first-motion solutions (Bayasgalan et al., 2005). Global Positioning System (GPS)-derived crustal motion with respect to Eurasia in green (Calais et al., 2003). (c) Geological and structural map around the Bulnay fault system, modified from the Geological Map of Mongolia at a scale of 1:1,000,000 (Institute of Geology and Mineral Resources of the Mongolian Academy of Sciences, 1998). Coseismic surface breaks associated with the 1905 Tsetserleg-Bulnay earthquake sequence are in red, according to our mapping.

earthquakes constitute the largest continental strike-slip earthquake sequence ever documented. The two successive events, which we designate as the 1905 Tsetserleg-Bulnay earthquakes (T-B EQs), together ruptured fault sections along the main Bulnay fault as well as along three other major faults: the Tsetserleg fault, the Teregtiyn fault, and the Dungen fault (Figure 1c). The total length of surface breaks associated to this earthquake sequence is at least 676 km. Despite the fact that the 1905 T-B EQs surface ruptures are well preserved up to the present, it had only been mapped in detail along limited sections (Rizza et al., 2015).

In this paper we use submetric (pixel = 0.5 m) optical satellite images "Pleiades," complemented by two field-work campaigns, to map in detail the entire rupture zone associated with the 1905 T-B EQs. Wherever it was possible, we measured any lateral offsets along the different faults studied. Eventually, our results include both the 1905 coseismic deformation and cumulative deformations associated with previous events. Here we limit our focus only to the clearest data related to the 1905 sequence. Discussion of the cumulative deformation will be dealt with in a future paper. After a short overview of the regional tectonic context and of the methodologies used to achieve consistent mapping over the entire rupture, the different sections of the rupture are described to present characteristics of the deformation pattern. Eventually, rupture geometry and slip distributions are analyzed in the perspective of a better understanding of the interactions between rupture processes and structural parameters.

2. Seismotectonic and Geologic Settings

Four magnitude M ≥ 8 earthquakes happened between 1905 and 1957 in western Mongolia, respectively, along the faults of Bulnay, Bogd, and Fuyun (Baljinnyam et al., 1993; Figure 1b). Hence, Mongolia has been

regarded as one of the most tectonically active intracontinental regions in the world. These earthquakes are associated with the regional deformation related to the India-Eurasia convergence (Molnar & Tapponnier, 1975; Tapponnier & Molnar, 1979). Global Positioning System (GPS) data yield a total slip rate of about 4 mm/yr distributed across these different faults, from the south of the Gobi-Altay to the north of the Bulnay fault systems (Calais et al., 2003; Figure 1b). Surface ruptures associated with each earthquake are dominated by strike-slip motion over a distance of several hundred kilometers, with an average surface slip in excess of several meters in each case (Baljinnyam et al., 1993; Khil'ko et al., 1985; Kurushin et al., 1997). Recent studies of the surface ruptures associated with the 1931 Fuyun earthquake and the 1957 Gobi-Altay earthquake, based on their geomorphological expressions, suggested that these fault sections had experienced repeated surface-rupturing earthquakes over a period of 10^4–10^5 ka (Nissen et al., 2009; Ritz et al., 1995, 2006; Vassallo et al., 2007; Walker et al., 2006). Recurrence time for these events are on the order of thousands of years, and the ruptures exhibit characteristic-slip type of earthquakes (Klinger et al., 2011; Rizza et al., 2011). The four $M \geq 8$ earthquakes between 1905 and 1957, which constitute a sequence of exceptionally large earthquakes during a short time interval, have been interpreted as an evidence of potential mechanical interaction between faults located at large distances (at least ~400 km) from each other (Chery et al., 2001; Pollitz et al., 2003).

The 1905 T-B EQs occurred on the Bulnay (or Northern Hangay) fault system, which extends east-west along the northern slope of the Hangay dome (Figure 1b). The main fault of the system, the Bulnay fault, is characterized by a ~600 km long fault strand with an average azimuth of 96°. The Bulnay fault is primarily located along the Mesozoic suture associated with the closure of the Mongolian-Okhotsk Ocean and partly follows older fault contacts between different Early Paleozoic allochthonous terranes (Badarch et al., 2002; Jolivet et al., 2007; Figure 1c). A total left-lateral offset of ~50 km is measured from displaced Paleozoic bedrock units (Zonenshein, 1973), whereas only several kilometers of cumulative offsets were observed based on displaced large rivers, such as Galutu rivers (4 ± 0.5 km) (Rizza et al., 2015; Walker et al., 2008). Along the eastern part of the Bulnay fault Rizza et al. (2015) have proposed that the slip rate is 3.1 ± 1.7 mm/yr for the Late Pleistocene-Holocene period, based on cumulative offset of streams and alluvial surfaces. Paleoseismological investigations at two sites (approximately 200 km apart) along the Bulnay fault, which ruptured during the 1905 T-B EQs, suggested that the penultimate surface rupture event at each site occurred 2,480–3,270 cal. before present and 2,300–3,250 cal. before present, respectively (Rizza et al., 2015; Schwartz et al., 2009).

Much of the surface rupture associated with the 1905 T-B EQs has been recognized during several field explorations that started as early as mid-September 1905 and lasted for 10 years (Voznesenskii, 1962; Voznesenskii & Dorogostaiskii, 1914). The ground rupture along the Teregtiyn fault was only discovered 50 years after the events (Aprodov, 1960). During these early investigations, each surface rupture was assigned either to the Tsetserleg or to the Bulnay event, according to the reports of local people (Voznesenskii, 1962). In the late 1980s, Khil'ko et al. (1985) and Baljinnyam et al. (1993) provided a first-order rupture map of the 1905 T-B EQs, including coseismic slip data at several locations. Combining rupture parameters and body waveform inversion for the 1905 T-B EQs, Schlupp and Cisternas (2007) suggested that (1) although an approximately 130 km long rupture has been observed along the Tsetserleg fault in the field, its total length may have reached up to ~190 km, that is, an additional ~60 km long rupture northeastward, to account for a difference between geologically and seismologically calculated seismic moments; and (2) the Bulnay rupture initiated at the junction area between the Bulnay and Teregtiyn faults and then propagated into three directions, with the main rupture eastward along the Bulnay fault. An additional rupture was also recognized onto the Dungen fault.

3. High-Resolution Satellite Imagery Mapping

We used Pleiades high-resolution satellite (HRS) images, which have a ground resolution of 0.5 m, to map the 1905 T-B EQs surface ruptures. This data set covers all of the reported major rupture traces as well as surrounding areas (within 2 km perpendicular to the main rupture strands). The data set has been complemented, when needed, by freely available web-based HRS images (e.g., Google Maps and Bing Maps). Our mapping results include secondary ruptures (>0.5 m of width) where they are still preserved (Figure 2). Many of these geometric features had not been recognized before, as a systematic field exploration over

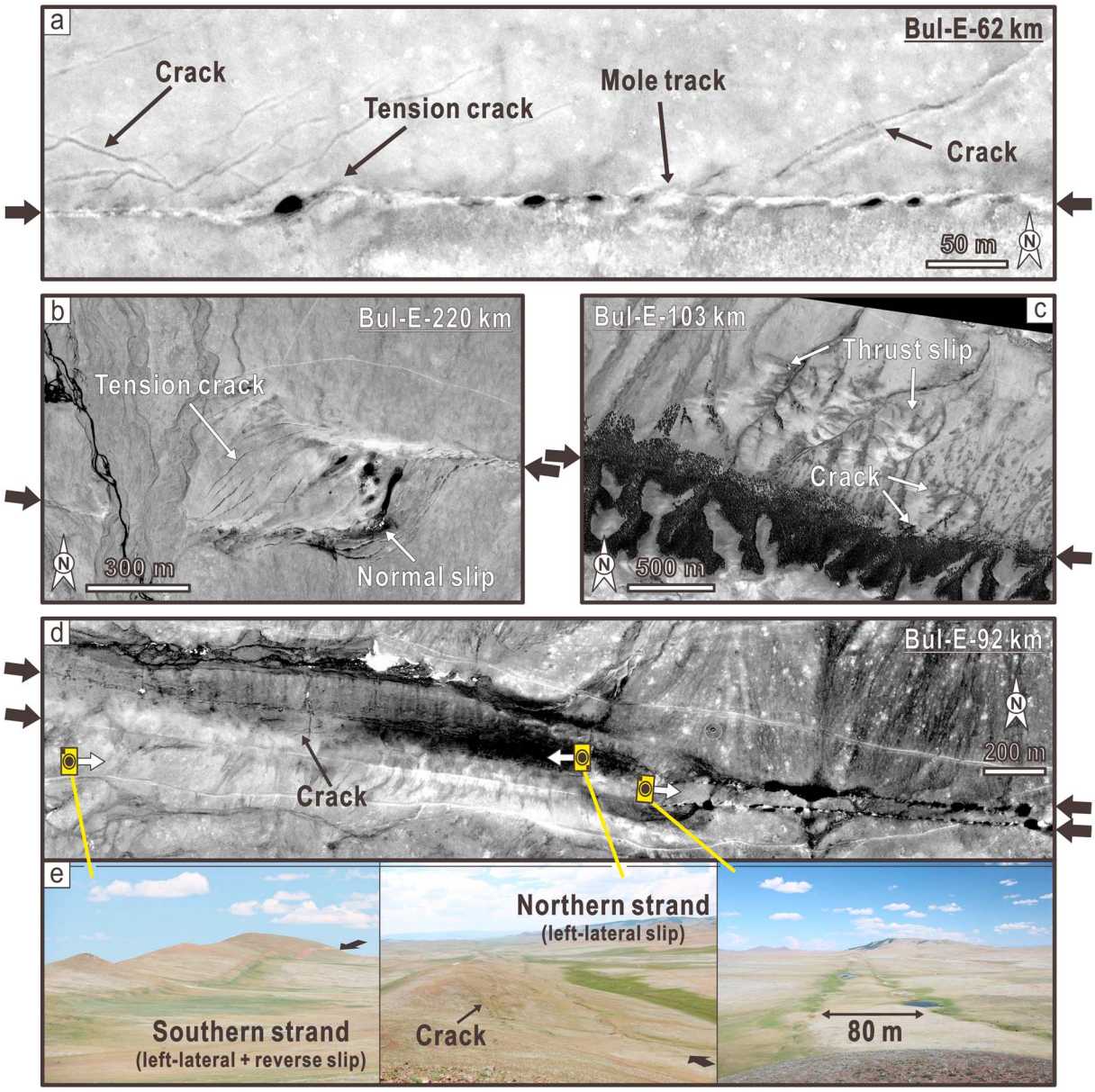

Figure 2. (a–d) Examples of surface ruptures associated with the 1905 Bulnay earthquake imaged by submetric optical satellite images Pleiades (ground resolution of 0.5 m): (a) main rupture strand consisting of en echelon tension cracks and mole tracks, (b) pull-apart geometry associated with a step of two parallel faults, (c) local compressional deformation associated with a change in azimuth of the main fault, and (d) two parallel strike-slip rupture strands. In all examples, secondary cracks are distributed around the main rupture strand. (e) Field views of similar complexities.

the entire rupture, to identify all secondary ruptures, would have required time beyond availability. The rupture map, containing all the ground ruptures associated to the 1905 events, as well as tectonic scarps next to the 1905 coseismic deformations, is provided in Data Set S1 in the supporting information.

Using HRS imagery, we were also able to estimate horizontal offsets by reconstruction of pre-earthquake geomorphology (back slip) (Figure 3). Most of the offsets were estimated using piercing lines that intersect the rupture, such as stream channels, thalwegs, or terrace risers. Because we could not access vertical deformation from HRS imagery alone, when measuring offsets we tried to use piercing lines making an angle as close as possible to 90° with the rupture trace. Doing so, we limited as much as possible bias in our measurements due to introduction of apparent horizontal offsets related to dip-slip motion of an oblique piercing line (Elliott et al., 2012). Because we have no observations about the morphology before the 1905 earthquake, we have systematically measured all well-defined geomorphic offsets along the recognized

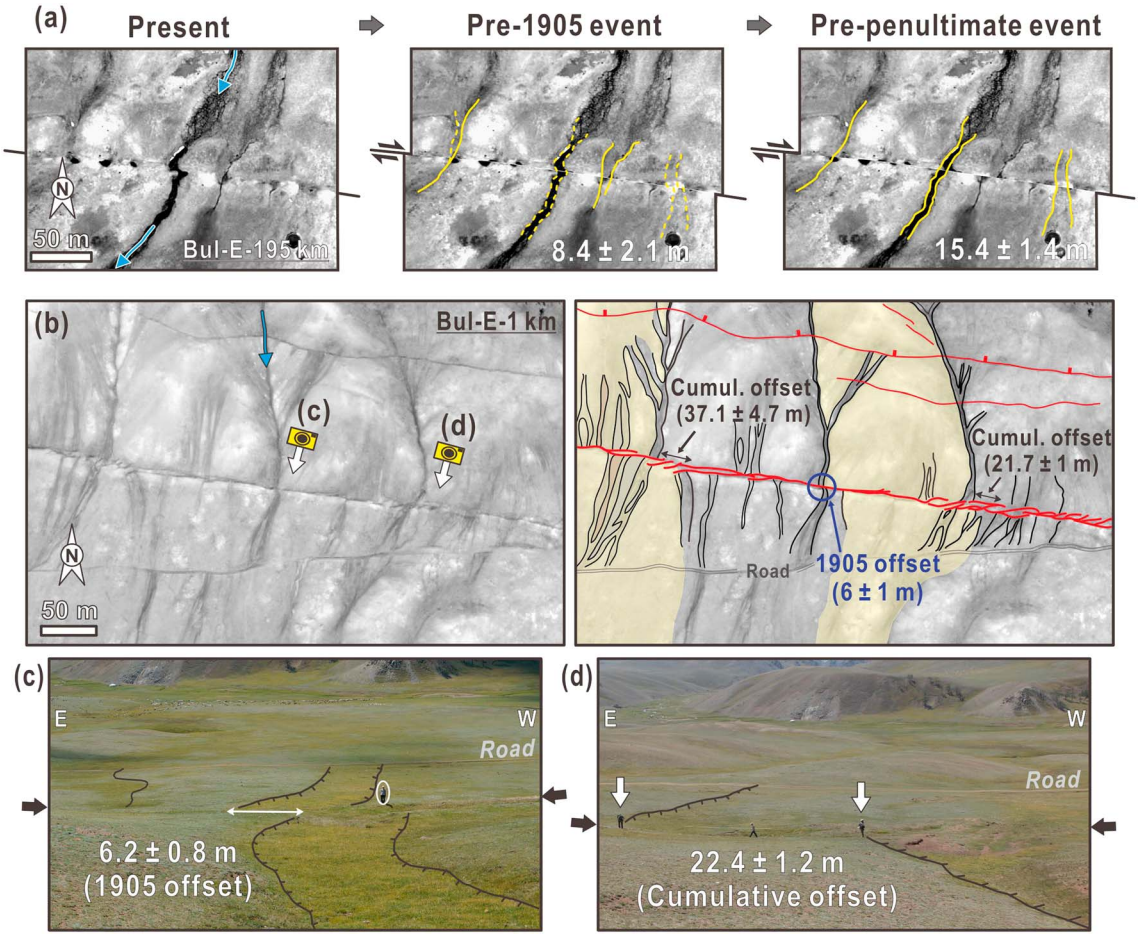

Figure 3. (a, b) Offset measurements using the high-resolution satellite image. Drainages nearly perpendicular to the fault provide good piercing lines to estimate both 1905 coseismic and cumulative horizontal offsets. In Figure 3a, preearthquake morphology is marked by solid lines, whereas postearthquake morphology is indicated by dashed lines. (c, d) Offset measurements in the field to cross-check our imagery mapping. Note that, for the same site, estimated slip values based on high-resolution satellite images and field observations are indistinguishable.

ruptures. In total, we have collected a data set of 654 offsets at 384 sites: at 184 sites we could measure only one offset, and at 200 sites we could measure multiple offsets. Accuracy of each offset has been assessed by (1) quantitative estimate of maximum, minimum, and preferred values for reconstruction of each piercing line and (2) qualitative ranking: high, intermediate, or low, based on five criteria that are marker width, marker straightness/sinuosity, rupture zone width, distance between marker and rupture, and visibility of markers on images (Figure S1). To rank our data, we scored each observation according to the listed criteria following the scheme: 3 points for *high quality*, 2 points for *intermediate quality*, and 1 point to *low quality* (see the Table 1 and Figure S1 for details). Eventually, adding points obtained for each criteria, each datum is ranked: An observation scoring between 15 and 13 points is deemed *high quality*, between 12 and 10 points, *intermediate quality*, and less than 10 points, *low quality*. All the scoring information is included in Table 1.

Our data set is divided in two parts: The first part corresponds to the 1905 coseismic slip and the second part includes cumulative slip measurements. At this stage, we assumed that only the smallest offset at each site (384 sites in total) corresponds with the 1905 coseismic slip, which was selected to be part of our first sub–data set. Any larger offset measured at the same site was considered as cumulative offset and ended up in the second sub–data set. Next, although we acknowledge that some significant variability of coseismic slip over short distances might exist (Rockwell et al., 2002; Rockwell & Klinger, 2013; Vallage et al., 2015), we also discarded any offset that shows unrealistic slip variation over a short distance, assuming that for some reasons the 1905 coseismic offset was not preserved at that site and that the offset measured actually

Table 1
Coseismic Horizontal Offset on Individual Major Faults Activated During the 1905 T-B EQs Surface Rupture From HRS Measurements

Locality			Geomorphic offset marker							
				Data quality[b]						
No.[a]	Latitude	Longitude	Type	OMW	OMS	RZW	PZW	IQ	Summation	Horizontal Offset (m)
Tsetserleg rupture (southwestern section)										
−31.3	49°23′0.45″	97°2′12.70″	Gully	I (2)	I (2)	I (2)	I (2)	H (3)	I (11)	1.8 ± 0.3
−30.2	49°23′16.85″	97°3′2.50″	Gully, Riser	I (2)	I (2)	I (2)	I (2)	H (3)	I (11)	1.5 ± 0.4
Tsetserleg rupture (central section)										
−3	49°30′45.30″	97°20′6.42″	Alluvial fan, Gully	H (3)	I (2)	I (2)	I (2)	H (3)	I (12)	2.1 ± 0.4
−2.4	49°30′53.21″	97°20′34.53″	Gully	I (2)	I (2)	H (3)	L (1)	I (2)	I (10)	3.0 ± 0.4
0	49°31′27.71″	97°22′20.98″	Gully	H (3)	I (2)	I (2)	I (2)	I (2)	I (11)	2.5 ± 0.4
0.8	49°31′39.81″	97°22′56.58″	Gully	I (2)	I (2)	I (2)	H (3)	L (1)	I (10)	2.1 ± 0.4
1.5	49°31′49.68″	97°23′27.66″	Gully, Riser	H (3)	I (2)	I (2)	I (2)	H (3)	I (12)	1.6 ± 0.2
2.2	49°32′4.54″	97°23′51.70″	Alluvial fan, Gully	I (2)	I (2)	I (2)	I (2)	I (2)	I (10)	2.2 ± 0.3
2.7	49°32′14.65″	97°24′15.08″	Gully	I (2)	I (2)	I (2)	I (2)	I (2)	I (10)	2.6 ± 0.4
3.2	49°32′23.87″	97°24′35.10″	Gully	H (3)	I (2)	I (2)	L (1)	H (3)	I (11)	2.9 ± 0.5
5.6	49°32′57.09″	97°26′25.17″	Gully	H (3)	I (2)	H (3)	I (2)	H (3)	H (13)	2.2 ± 0.3
8.3	49°34′0.04″	97°27′58.65″	Alluvial fan, Gully	I (2)	I (2)	I (2)	L (1)	H (3)	I (10)	3.0 ± 0.6
8.5 (s)	49°33′33.04″	97°28′11.28″	Gully	H (3)	I (2)	I (2)	I (2)	H (3)	I (12)	1.2 ± 0.5
10.1 (s)	49°34′17.50″	97°29′28.10″	Gully	H (3)	I (2)	H (3)	I (2)	H (3)	H (13)	2.1 ± 0.4
11.8	49°34′59.82″	97°30′28.68″	Gully	I (2)	I (2)	H (3)	I (2)	H (3)	I (12)	3.2 ± 0.5
13.3	49°35′21.32″	97°31′35.75″	Gully	I (2)	I (2)	H (3)	I (2)	H (3)	I (12)	2.9 ± 0.5
13.7	49°35′25.78″	97°31′55.15″	Gully	I (2)	I (2)	H (3)	H (3)	H (3)	H (13)	3.0 ± 0.5
15.2	49°35′48.75″	97°32′59.35″	Gully, Riser	I (2)	I (2)	H (3)	I (2)	H (3)	I (12)	2.9 ± 0.6
15.6	49°35′53.04″	97°33′19.40″	Gully, Riser	I (2)	I (2)	H (3)	I (2)	H (3)	I (12)	2.5 ± 0.3
17.3	49°36′14.03″	97°34′38.76″	Gully	H (3)	I (2)	I (2)	H (3)	H (3)	H (13)	2.5 ± 0.4
26.2	49°39′6.39″	97°40′38.04″	Gully	H (3)	I (2)	I (2)	I (2)	H (3)	I (12)	3.3 ± 0.7
28.1	49°39′45.97″	97°41′53.51″	Gully	I (2)	I (2)	I (2)	I (2)	I (2)	I (10)	2.9 ± 0.7
30.5	49°40′26.73″	97°43′5.60″	Gully, Riser	I (2)	I (2)	H (3)	I (2)	H (3)	I (12)	3.3 ± 0.5
Bulnay rupture (western end section)										
−57.7	49°24′15.23″	94°4′46.67″	Gully, Riser	I (2)	I (2)	H (3)	I (2)	I (2)	I (11)	1.2 ± 0.3
Bulnay rupture (section-A)										
−43.6	49°23′24.06″	94°16′23.30″	Gully	I (2)	I (2)	H (3)	H (3)	H (3)	H (13)	1.7 ± 0.2
−38.4	49°23′23.20″	94°20′39.13″	Terrace Riser	I (2)	H (3)	I (2)	L (1)	H (3)	I (11)	2.8 ± 0.2
−34.8	49°23′18.05″	94°23′38.56″	Gully	I (2)	I (2)	I (2)	I (2)	H (3)	I (11)	2.4 ± 0.7
−34.3	49°23′18.33″	94°24′4.20″	Gully	I (2)	H (3)	I (2)	I (2)	H (3)	I (12)	2.1 ± 0.4
−30.8	49°23′5.88″	94°26′57.77″	Stream, Riser	I (2)	I (2)	H (3)	H (3)	H (3)	H (13)	3.2 ± 1.0
Bulnay rupture (section-B)										
−22	49°22′36.73″	94°34′10.45″	Stream	I (2)	H (3)	H (3)	I (2)	H (3)	H (13)	3.8 ± 1.2
−21.5	49°22′34.22″	94°34′32.56″	Stream	I (2)	I (2)	H (3)	I (2)	H (3)	I (12)	4.0 ± 0.6
−20.9	49°22′30.47″	94°35′5.81″	Stream	I (2)	H (3)	H (3)	I (2)	H (3)	H (13)	3.8 ± 0.7
−20.2	49°22′26.20″	94°35′40.05″	Gully	I (2)	H (3)	H (3)	I (2)	H (3)	H (13)	3.4 ± 0.6
−19.9	49°22′24.54″	94°35′52.00″	Gully	I (2)	I (2)	H (3)	I (2)	H (3)	I (12)	3.6 ± 0.8
−19.8	49°22′23.76″	94°35′58.61″	Mt. Ridge, Gully	I (2)	H (3)	H (3)	I (2)	H (3)	H (13)	3.7 ± 0.6
−19.6	49°22′22.95″	94°36′5.46″	Mt. Ridge, Gully	I (2)	H (3)	H (3)	I (2)	H (3)	H (13)	3.9 ± 0.7
−19.1	49°22′19.32″	94°36′29.68″	Gullies	I (2)	I (2)	H (3)	I (2)	H (3)	I (12)	3.9 ± 0.4
−18.6	49°22′15.13″	94°36′57.58″	Mt. Ridge, Gully	I (2)	H (3)	H (3)	I (2)	H (3)	H (13)	4.4 ± 1.0
−18.4	49°22′14.10″	94°37′6.66″	Gully	I (2)	H (3)	H (3)	I (2)	H (3)	H (13)	4.7 ± 0.2
−17.3	49°22′6.66″	94°37′56.98″	Gully	I (2)	H (3)	H (3)	I (2)	H (3)	H (13)	4.8 ± 0.6
−16.5	49°22′0.42″	94°38′36.04″	Stream	I (2)	H (3)	H (3)	I (2)	H (3)	H (13)	4.7 ± 0.7
−15.9	49°21′54.87″	94°39′6.51″	Mt. Ridge, Gully	I (2)	H (3)	H (3)	I (2)	H (3)	H (13)	4.7 ± 0.6
−15.4	49°21′51.61″	94°39′27.49″	Mt. Ridge, Gully	I (2)	I (2)	H (3)	I (2)	H (3)	I (12)	5.0 ± 0.5
−15.3	49°21′50.12″	94°39′35.28″	Mt. Ridge, Gully	I (2)	H (3)	H (3)	I (2)	H (3)	H (13)	4.3 ± 0.9
−15	49°21′48.11″	94°39′46.35″	Mt. Ridge, Gully	I (2)	H (3)	H (3)	I (2)	H (3)	H (13)	4.0 ± 0.4
−14.6	49°21′44.13″	94°40′6.30″	Mt. Ridge, Gully	I (2)	H (3)	H (3)	I (2)	H (3)	H (13)	5.1 ± 1.2
−14.1	49°21′39.20″	94°40′31.25″	Mt. Ridge, Gully	I (2)	I (2)	H (3)	I (2)	H (3)	I (12)	4.7 ± 0.6
−13.8	49°21′37.34″	94°40′46.42″	Mt. Ridge, Gully	I (2)	H (3)	H (3)	I (2)	H (3)	H (13)	4.9 ± 0.4
−13.5	49°21′35.32″	94°41′2.87″	Mt. Ridge, Gully	I (2)	I (2)	H (3)	I (2)	H (3)	I (12)	4.9 ± 0.8
−13.1	49°21′33.39″	94°41′19.46″	Mt. Ridge, Gully	I (2)	H (3)	H (3)	I (2)	H (3)	H (13)	4.1 ± 0.9
−8.9	49°21′11.30″	94°44′38.08″	Stream, Terrace Riser	H (3)	I (2)	H (3)	H (3)	H (3)	H (14)	3.4 ± 0.5
−7.8	49°21′4.94″	94°45′40.63″	Gully, Riser	I (2)	H (3)	I (2)	I (2)	H (3)	I (12)	4.4 ± 0.4

Table 1 *(continued)*

Locality			Geomorphic offset marker							
				Data quality[b]						
No.[a]	Latitude	Longitude	Type	OMW	OMS	RZW	PZW	IQ	Summation	Horizontal Offset (m)
−7.4	49°21′2.43″	94°46′1.06″	Gully, Riser	I (2)	I (2)	I (2)	I (2)	H (3)	I (11)	4.1 ± 0.7
−6.6	49°20′57.19″	94°46′39.44″	Gully	I (2)	I (2)	I (2)	I (2)	H (3)	I (11)	3.9 ± 0.8
−5.3	49°20′47.74″	94°47′39.24″	Gully	I (2)	H (3)	I (2)	I (2)	H (3)	I (12)	4.0 ± 0.5
−1.7	49°20′28.58″	94°50′39.62″	Gully	I (2)	L (1)	I (2)	L (1)	I (2)	L (8)	3.8 ± 0.3
Bulnay rupture (section-C)										
0.8	49°20′12.96″	94°52′38.51″	Gully	H (3)	I (2)	I (2)	H (3)	H (3)	H (13)	5.5 ± 0.4
0.9	49°20′12.20″	94°52′44.90″	Gullies	I (2)	H (3)	I (2)	I (2)	H (3)	I (12)	5.9 ± 0.7
1.1	49°20′10.89″	94°52′53.93″	Gully	H (3)	I (2)	I (2)	I (2)	H (3)	I (12)	5.5 ± 0.5
1.2	49°20′10.40″	94°52′57.83″	Gully	H (3)	I (2)	H (3)	I (2)	H (3)	H (13)	6.0 ± 1.0
1.4	49°20′9.59″	94°53′6.57″	Gully	H (3)	H (3)	I (2)	I (2)	H (3)	H (13)	6.1 ± 0.5
9.5	49°19′42.05″	94°59′50.13″	Gully	H (3)	H (3)	I (2)	L (1)	L (1)	I (10)	6.6 ± 1.0
10.5	49°19′36.58″	95°0′39.00″	Gully	I (2)	H (3)	I (2)	I (2)	I (2)	I (11)	6.3 ± 0.5
11.9	49°19′24.50″	95°1′44.75″	Gully	H (3)	L (1)	H (3)	H (3)	H (3)	H (13)	6.4 ± 0.6
12	49°19′24.34″	95°1′48.61″	Gully	I (2)	I (2)	I (2)	I (2)	H (3)	I (11)	6.9 ± 0.7
18.9	49°18′35.78″	95°7′20.86″	Gully	I (2)	I (2)	H (3)	I (2)	H (3)	I (12)	6.4 ± 1.4
25.1	49°17′54.75″	95°12′22.92″	Gully	L (1)	I (2)	I (2)	I (2)	H (3)	I (10)	6.3 ± 1.7
26.5	49°17′50.90″	95°13′30.50″	Gully	L (1)	H (3)	L (1)	L (1)	H (3)	L (9)	7.0 ± 1.2
27	49°17′48.13″	95°13′55.58″	Gully	I (2)	I (2)	L (1)	I (2)	H (3)	I (10)	7.0 ± 1.0
27.5	49°17′46.37″	95°14′20.34″	Gully	I (2)	I (2)	L (1)	I (2)	H (3)	I (10)	6.9 ± 0.7
28.6	49°17′44.22″	95°15′13.63″	Gully	H (3)	I (2)	I (2)	H (3)	H (3)	H (13)	6.7 ± 1.1
28.9	49°17′43.74″	95°15′29.83″	Terraces, Gully	L (1)	H (3)	I (2)	L (1)	H (3)	I (10)	6.8 ± 1.0
29.4	49°17′42.78″	95°15′55.42″	Gully	I (2)	I (2)	I (2)	L (1)	H (3)	I (10)	7.2 ± 0.7
32.1	49°17′37.42″	95°18′6.56″	Gullies	H (3)	I (2)	I (2)	H (3)	H (3)	H (13)	7.3 ± 0.3
32.3	49°17′36.79″	95°18′17.20″	Gully	H (3)	I (2)	I (2)	H (3)	H (3)	H (13)	7.5 ± 1.0
33.2 (s)	49°17′30.43″	95°19′4.02″	Gully	L (1)	H (3)	H (3)	I (2)	H (3)	I (12)	1.1 ± 0.3
33.3	49°17′32.65″	95°19′5.30″	Gully	I (2)	I (2)	I (2)	I (2)	H (3)	I (11)	7.1 ± 0.6
34.3	49°17′28.79″	95°19′57.06″	Gully	I (2)	H (3)	I (2)	L (1)	H (3)	I (11)	6.1 ± 1.0
34.8	49°17′26.83″	95°20′23.44″	Gully	H (3)	I (2)	I (2)	I (2)	H (3)	I (12)	6.4 ± 0.4
35.1	49°17′25.41″	95°20′36.36″	Gully	I (2)	I (2)	L (1)	I (2)	H (3)	I (10)	6.3 ± 0.6
35.3	49°17′24.36″	95°20′43.95″	Gully	I (2)	I (2)	L (1)	L (1)	H (3)	L (9)	6.4 ± 0.5
35.7	49°17′22.22″	95°21′4.47″	Gully	I (2)	I (2)	L (1)	I (2)	H (3)	I (10)	6.5 ± 0.6
36.8	49°17′17.93″	95°21′58.06″	Gully	H (3)	H (3)	I (2)	H (3)	H (3)	H (14)	6.2 ± 1.1
37.5	49°17′15.11″	95°22′31.52″	Gully	H (3)	I (2)	L (1)	I (2)	H (3)	I (11)	4.3 ± 0.6
39.2	49°17′7.40″	95°23′54.70″	Gully	I (2)	H (3)	I (2)	I (2)	H (3)	I (12)	4.7 ± 0.7
39.5	49°17′5.77″	95°24′10.97″	Gully	I (2)	I (2)	I (2)	I (2)	H (3)	I (11)	5.0 ± 0.8
40	49°17′3.74″	95°24′34.34″	Gully	I (2)	I (2)	I (2)	H (3)	H (3)	I (12)	3.2 ± 0.4
40.2	49°17′2.58″	95°24′44.73″	Gully	H (3)	I (2)	I (2)	H (3)	H (3)	H (13)	3.1 ± 0.2
41.2	49°16′58.79″	95°25′33.79″	Gully, Riser	H (3)	L (1)	I (2)	I (2)	H (3)	I (11)	3.8 ± 0.7
Bulnay rupture (section-D)										
47 (s)	49°16′38.24″	95°30′19.29″	Gully	H (3)	H (3)	H (3)	H (3)	H (3)	H (15)	3.2 ± 0.4
47.3	49°16′36.89″	95°30′33.69″	Gully	I (2)	I (2)	I (2)	H (3)	H (3)	I (12)	3.3 ± 0.3
47.7	49°16′35.43″	95°30′54.65″	Gully	I (2)	I (2)	L (1)	L (1)	H (3)	L (9)	3.9 ± 0.6
47.9	49°16′33.90″	95°31′6.60″	Gully	I (2)	I (2)	I (2)	L (1)	H (3)	I (10)	4.5 ± 0.6
48.5	49°16′30.73″	95°31′33.05″	Gully	H (3)	I (2)	H (3)	H (3)	H (3)	H (14)	5.2 ± 0.4
48.7	49°16′29.31″	95°31′41.24″	Gully	H (3)	I (2)	I (2)	I (2)	H (3)	I (12)	5.2 ± 0.5
48.8	49°16′28.50″	95°31′45.64″	Gullies	H (3)	I (2)	I (2)	I (2)	H (3)	I (12)	5.6 ± 0.6
48.9	49°16′27.28″	95°31′54.83″	Gully	H (3)	I (2)	L (1)	I (2)	H (3)	I (11)	6.6 ± 0.7
54.2	49°16′21.81″	95°36′13.87″	Gully	I (2)	I (2)	I (2)	L (1)	I (2)	L (9)	7.0 ± 1.2
57.4	49°16′17.39″	95°38′52.69″	Gully	I (2)	I (2)	I (2)	I (2)	H (3)	I (11)	6.3 ± 0.6
62.2	49°16′15.16″	95°42′49.90″	Gully	I (2)	I (2)	I (2)	I (2)	H (3)	I (11)	6.3 ± 1.0
65.5 (s)	49°16′32.88″	95°45′33.91″	Gullies	H (3)	L (1)	H (3)	I (2)	H (3)	I (12)	1.4 ± 0.6
65.6	49°16′14.31″	95°45′39.02″	Gully, Riser	L (1)	I (2)	I (2)	L (1)	H (3)	L (9)	6.4 ± 0.7
66.2	49°16′13.53″	95°46′6.89″	Gully, Riser	L (1)	L (1)	I (2)	I (2)	H (3)	L (9)	6.9 ± 1.4
71.5	49°16′9.93″	95°50′28.39″	Gully	L (1)	L (1)	I (2)	I (2)	H (3)	L (9)	7.1 ± 0.8
74.4 (s)	49°16′19.37″	95°52′50.81″	Gully	I (2)	I (2)	I (2)	H (3)	H (3)	I (12)	2.5 ± 0.3
76.01 (s)	49°16′11.37″	95°54′13.73″	Gully	H (3)	I (2)	H (3)	I (2)	H (3)	H (13)	2.6 ± 0.8
76.03	49°16′5.37″	95°54′14.39″	Gully, Riser	L (1)	L (1)	L (1)	I (2)	H (3)	L (8)	5.2 ± 0.6

Table 1 *(continued)*

Locality			Geomorphic offset marker							
				Data quality[b]						
No.[a]	Latitude	Longitude	Type	OMW	OMS	RZW	PZW	IQ	Summation	Horizontal Offset (m)
76.66 (s)	49°16′9.73″	95°54′45.86″	Gully	I (2)	I (2)	I (2)	I (2)	H (3)	I (11)	2.8 ± 0.4
76.72 (s)	49°16′9.69″	95°54′49.25″	Gullies	I (2)	I (2)	I (2)	L (1)	H (3)	I (10)	2.8 ± 0.7
77.41 (s)	49°16′4.89″	95°55′23.76″	Gullies	H (3)	I (2)	I (2)	H (3)	H (3)	H (13)	1.7 ± 0.3
77.42 (s)	49°16′9.17″	95°55′23.99″	Gully, Riser	I (2)	I (2)	I (2)	I (2)	H (3)	I (11)	1.3 ± 0.6
Bulnay rupture (section-E)										
79.7	49°16′3.66″	95°57′18.69″	Gullies	I (2)	I (2)	L (1)	L (1)	H (3)	L (9)	5.5 ± 0.8
81.1	49°16′0.48″	95°58′23.02″	Gully	H (3)	L (1)	I (2)	L (1)	H (3)	I (10)	5.5 ± 0.7
81.97 (s)	49°15′53.05″	95°59′7.65″	Gully	H (3)	H (3)	I (2)	H (3)	H (3)	H (14)	1.8 ± 0.4
82.03	49°15′58.48″	95°59′11.19″	Gullies	I (2)	H (3)	I (2)	I (2)	H (3)	I (12)	4.1 ± 0.4
82.2	49°15′57.77″	95°59′20.21″	Gullies	H (3)	H (3)	I (2)	I (2)	H (3)	H (13)	4.7 ± 0.5
82.3 (s)	49°15′52.07″	95°59′25.75″	Gully	H (3)	I (2)	H (3)	H (3)	H (3)	H (14)	1.7 ± 0.2
82.4	49°15′57.33″	95°59′30.09″	Gullies	I (2)	H (3)	I (2)	I (2)	H (3)	I (12)	4.9 ± 0.7
83.1	49°15′55.21″	96°0′3.89″	Gullies	I (2)	I (2)	I (2)	I (2)	H (3)	I (11)	4.2 ± 0.3
83.3	49°15′54.91″	96°0′11.58″	Gullies	H (3)	I (2)	L (1)	L (1)	H (3)	I (10)	4.0 ± 0.6
83.8	49°15′53.30″	96°0′39.84″	Gully	I (2)	I (2)	I (2)	L (1)	H (3)	I (10)	5.0 ± 0.4
83.9 (s)	49°15′46.32″	96°0′40.75″	Gully	H (3)	I (2)	H (3)	H (3)	H (3)	H (14)	2.1 ± 0.5
84.2 (s)	49°15′45.27″	96°0′58.90″	Gully	I (2)	L (1)	H (3)	H (3)	H (3)	I (12)	1.8 ± 0.2
84.3	49°15′51.79″	96°1′0.64″	Gullies	I (2)	L (1)	I (2)	I (2)	H (3)	I (10)	4.8 ± 0.3
86.2 (s)	49°15′41.93″	96°2′37.39″	Gullies	I (2)	I (2)	H (3)	I (2)	H (3)	I (12)	2.0 ± 0.4
87.5	49°15′42.62″	96°3′39.20″	Gully	H (3)	L (1)	H (3)	I (2)	H (3)	I (12)	5.9 ± 0.5
92.9	49°15′29.76″	96°8′6.90″	Gully	H (3)	I (2)	I (2)	H (3)	H (3)	H (13)	5.8 ± 1.2
94.5	49°15′31.13″	96°9′28.45″	Gully	I (2)	H (3)	I (2)	H (3)	H (3)	H (13)	3.8 ± 0.8
95.3	49°15′28.11″	96°10′5.24″	Gullies	I (2)	I (2)	H (3)	H (3)	H (3)	H (13)	4.2 ± 1.0
95.4	49°15′23.12″	96°10′7.17″	Gully	I (2)	I (2)	L (1)	I (2)	H (3)	I (10)	5.1 ± 1.9
97 (s)	49°15′23.96″	96°11′30.69″	Gully	H (3)	I (2)	H (3)	H (3)	H (3)	H (14)	2.5 ± 0.4
97.1	49°15′19.14″	96°11′32.36″	Gully	I (2)	I (2)	I (2)	H (3)	H (3)	I (12)	5.0 ± 0.7
97.86 (s)	49°15′22.18″	96°12′11.24″	Gullies	I (2)	I (2)	H (3)	H (3)	H (3)	H (13)	3.7 ± 0.2
97.94	49°15′17.00″	96°12′14.84″	Gullies	L (1)	I (2)	I (2)	L (1)	I (2)	L (8)	5.3 ± 1.1
Bulnay rupture (section-F)										
105.5	49°14′48.66″	96°18′26.88″	Gully	I (2)	I (2)	I (2)	L (1)	H (3)	I (10)	5.2 ± 0.9
105.7	49°14′47.50″	96°18′33.17″	Gully	I (2)	H (3)	I (2)	H (3)	H (3)	H (13)	5.4 ± 0.7
106	49°14′47.57″	96°18′52.93″	Gullies	I (2)	I (2)	L (1)	I (2)	H (3)	I (10)	5.9 ± 1.4
106.5	49°14′45.30″	96°19′14.66″	Gully	I (2)	I (2)	I (2)	I (2)	H (3)	I (11)	5.8 ± 1.1
107.3	49°14′42.67″	96°19′55.71″	Gully	H (3)	H (3)	I (2)	L (1)	H (3)	I (12)	6.8 ± 1.0
107.6	49°14′41.92″	96°20′9.20″	Gully	H (3)	H (3)	I (2)	I (2)	H (3)	H (13)	6.8 ± 0.4
107.9	49°14′41.02″	96°20′25.21″	Gullies	H (3)	I (2)	I (2)	I (2)	H (3)	I (12)	7.1 ± 1.1
108.3	49°14′39.80″	96°20′43.20″	Gully, Track	I (2)	H (3)	I (2)	H (3)	H (3)	H (13)	6.3 ± 1.0
108.7	49°14′38.70″	96°21′3.91″	Gully, Track	I (2)	H (3)	I (2)	I (2)	H (3)	I (12)	6.0 ± 0.8
109.6	49°14′37.52″	96°21′22.66″	Gullies	H (3)	I (2)	I (2)	H (3)	H (3)	H (13)	6.7 ± 1.0
110	49°14′35.39″	96°22′5.76″	Gully	I (2)	I (2)	I (2)	I (2)	H (3)	I (11)	6.6 ± 1.6
112.7	49°14′28.96″	96°24′19.93″	Gullies	H (3)	I (2)	H (3)	H (3)	H (3)	H (14)	7.1 ± 1.7
113.3	49°14′27.79″	96°24′51.97″	Gully, Terrace	I (2)	H (3)	I (2)	H (3)	H (3)	H (13)	7.1 ± 1.4
114.9	49°14′24.12″	96°26′9.57″	Gullies, Terrace	H (3)	H (3)	I (2)	I (2)	H (3)	H (13)	7.7 ± 1.0
115.5	49°14′22.71″	96°26′41.05″	Gully	I (2)	I (2)	I (2)	I (2)	H (3)	I (11)	7.1 ± 0.6
115.9	49°14′21.83″	96°26′57.02″	Gully	H (3)	I (2)	H (3)	I (2)	H (3)	H (13)	7.7 ± 1.1
116.6	49°14′20.13″	96°27′35.01″	Gullies, Terrace	I (2)	H (3)	I (2)	H (3)	H (3)	H (13)	7.8 ± 1.0
117	49°14′18.61″	96°27′55.34″	Alluvial fan, Gully	I (2)	I (2)	H (3)	H (3)	H (3)	H (13)	8.0 ± 1.4
117.4	49°14′16.66″	96°28′16.01″	Alluvial fan, Gully	I (2)	I (2)	H (3)	H (3)	H (3)	H (13)	8.2 ± 1.3
117.7	49°14′15.79″	96°28′26.42″	Alluvial fan, Gully	I (2)	I (2)	H (3)	H (3)	H (3)	H (13)	8.3 ± 0.8
118.3	49°14′13.13″	96°28′56.62″	Alluvial fan	I (2)	H (3)	H (3)	H (3)	H (3)	H (14)	7.8 ± 1.5
118.6	49°14′12.14″	96°29′13.75″	Alluvial fan, Gully	I (2)	I (2)	H (3)	H (3)	H (3)	H (13)	7.8 ± 1.3
119.4	49°14′9.19″	96°29′51.92″	Alluvial fan, Gully	I (2)	I (2)	H (3)	H (3)	H (3)	H (13)	7.3 ± 1.0
119.9	49°14′7.72″	96°30′17.37″	Alluvial fan	H (3)	I (2)	H (3)	H (3)	H (3)	H (14)	7.7 ± 1.4
120.6	49°14′4.89″	96°30′48.00″	Gully	I (2)	H (3)	I (2)	H (3)	H (3)	H (13)	7.1 ± 0.9
120.8	49°14′4.21″	96°31′0.85″	Gully	I (2)	I (2)	H (3)	H (3)	H (3)	H (13)	7.7 ± 0.8
121.1	49°14′3.53″	96°31′13.67″	Gully	I (2)	I (2)	I (2)	H (3)	H (3)	I (12)	8.1 ± 1.2
124.2	49°13′59.19″	96°33′50.66″	Gully	I (2)	H (3)	I (2)	L (1)	H (3)	I (11)	7.9 ± 1.1

Table 1 *(continued)*

Locality			Geomorphic offset marker							
				Data quality[b]						
No.[a]	Latitude	Longitude	Type	OMW	OMS	RZW	PZW	IQ	Summation	Horizontal Offset (m)
131.37	49°13′47.31″	96°39′41.85″	Gullies	I (2)	I (2)	L (1)	I (2)	H (3)	I (10)	7.1 ± 0.9
134.4	49°13′46.53″	96°42′11.79″	Stream, Riser	L (1)	I (2)	I (2)	I (2)	H (3)	I (10)	7.6 ± 0.6
134.9	49°13′45.28″	96°42′38.89″	Gully, Sag-pond	L (1)	I (2)	I (2)	L (1)	H (3)	L (9)	7.5 ± 1.2
139.6	49°13′34.29″	96°46′28.74″	Alluvial fan, Gully	L (1)	I (2)	I (2)	L (1)	H (3)	L (9)	7.5 ± 1.3
140.6	49°13′32.04″	96°47′17.68″	Alluvial fan, Gully	L (1)	L (1)	I (2)	L (1)	I (2)	L (7)	7.1 ± 1.3
142	49°13′28.58″	96°48′29.08″	Alluvial fan, Gully	I (2)	I (2)	H (3)	H (3)	H (3)	H (13)	7.1 ± 1.6
142.3	49°13′28.02″	96°48′38.30″	Alluvial fan, Gully	I (2)	I (2)	H (3)	H (3)	H (3)	H (13)	7.0 ± 0.4
143	49°13′26.05″	96°49′17.23″	Alluvial fan, Gully	H (3)	H (3)	I (2)	I (2)	H (3)	H (13)	7.7 ± 0.9
143.4	49°13′25.08″	96°49′35.24″	Alluvial fan, Gully	H (3)	H (3)	I (2)	I (2)	H (3)	H (13)	7.3 ± 1.1
144.3	49°13′24.00″	96°50′18.36″	Terrace Riser	H (3)	H (3)	I (2)	I (2)	H (3)	H (13)	6.1 ± 1.4
144.5	49°13′23.40″	96°50′31.45″	Gully	I (2)	H (3)	I (2)	L (1)	H (3)	I (11)	6.3 ± 1.2
145.3	49°13′22.18″	96°51′11.96″	Gully	H (3)	L (1)	I (2)	I (2)	H (3)	I (11)	6.5 ± 1.3
148.4	49°13′10.96″	96°53′39.50″	Gully	I (2)	I (2)	L (1)	I (2)	H (3)	I (10)	3.2 ± 0.8
148.8	49°13′17.19″	96°54′2.54″	Gully	H (3)	I (2)	I (2)	I (2)	H (3)	I (12)	3.4 ± 0.4
Bulnay rupture (section-G)										
152.6	49°13′3.88″	96°57′7.36″	Gully	I (2)	I (2)	I (2)	H (3)	H (3)	I (12)	7.0 ± 1.0
160.8	49°12′35.27″	97°3′50.54″	Gully	H (3)	I (2)	I (2)	I (2)	H (3)	I (12)	7.7 ± 2.3
163.1	49°12′24.75″	97°5′35.00″	Gully	I (2)	I (2)	H (3)	H (3)	I (2)	I (12)	8.0 ± 1.6
171.5	49°11′37.46″	97°12′31.46″	Gullies	I (2)	I (2)	I (2)	I (2)	H (3)	I (11)	8.0 ± 1.8
172.1	49°11′34.53″	97°13′3.89″	Gully	H (3)	I (2)	I (2)	I (2)	H (3)	I (12)	8.6 ± 1.3
173.2	49°11′30.87″	97°13′55.86″	Gully	I (2)	L (1)	I (2)	L (1)	H (3)	L (9)	8.0 ± 1.5
175.1	49°11′21.99″	97°15′30.06″	Gully	I (2)	I (2)	I (2)	I (2)	H (3)	I (11)	9.0 ± 1.3
175.9	49°11′18.91″	97°16′6.86″	Gullies	I (2)	H (3)	I (2)	I (2)	H (3)	I (12)	8.8 ± 1.1
178.8	49°11′9.32″	97°18′30.32″	Gully	I (2)	I (2)	I (2)	I (2)	H (3)	I (11)	9.4 ± 0.8
180	49°11′4.07″	97°19′30.41″	Alluvial fan, Gully	I (2)	H (3)	I (2)	I (2)	H (3)	I (12)	9.7 ± 1.1
180.6	49°11′1.22″	97°20′1.11″	Alluvial fan, Gully	I (2)	H (3)	H (3)	I (2)	H (3)	H (13)	8.8 ± 1.4
181.8	49°10′55.92″	97°20′55.96″	Alluvial fan, Gully	I (2)	I (2)	I (2)	I (2)	H (3)	I (11)	9.1 ± 0.8
182.4	49°10′52.78″	97°21′26.49″	Alluvial fan, Gully	H (3)	I (2)	I (2)	H (3)	H (3)	H (13)	9.7 ± 1.6
182.7	49°10′51.25″	97°21′43.68″	Alluvial fan, Gully	I (2)	I (2)	H (3)	H (3)	H (3)	H (13)	10.1 ± 1.1
183.1	49°10′49.28″	97°22′2.67″	Alluvial fan, Gully	I (2)	I (2)	I (2)	I (2)	H (3)	I (11)	9.9 ± 0.8
183.6	49°10′47.19″	97°22′25.88″	Alluvial fan, Gully	H (3)	I (2)	I (2)	H (3)	H (3)	H (13)	9.5 ± 1.6
183.9	49°10′46.16″	97°22′37.84″	Gully	H (3)	I (2)	H (3)	I (2)	H (3)	H (13)	9.2 ± 1.1
184.6	49°10′43.12″	97°23′14.52″	Gully	H (3)	I (2)	H (3)	I (2)	H (3)	H (13)	8.6 ± 1.3
185	49°10′41.06″	97°23′35.14″	Gully	I (2)	H (3)	H (3)	I (2)	H (3)	H (13)	7.9 ± 1.2
186.1	49°10′36.49″	97°24′28.25″	Alluvial fan, Gully	I (2)	H (3)	I (2)	H (3)	H (3)	H (13)	6.5 ± 0.6
187	49°10′33.33″	97°25′11.83″	Gully	I (2)	I (2)	H (3)	I (2)	H (3)	I (12)	9.9 ± 1.7
188.3	49°10′29.14″	97°26′20.61″	Alluvial fan, Gully	I (2)	I (2)	I (2)	I (2)	H (3)	I (11)	10.4 ± 1.5
188.9	49°10′27.45″	97°26′46.57″	Gully	I (2)	I (2)	L (1)	I (2)	H (3)	I (10)	10.6 ± 0.8
192.1	49°10′19.02″	97°29′24.36″	Gully	I (2)	I (2)	I (2)	I (2)	H (3)	I (11)	10.3 ± 1.4
192.6	49°10′17.61″	97°29′48.95″	Gully	I (2)	H (3)	I (2)	H (3)	H (3)	H (13)	10.5 ± 1.8
193.6	49°10′14.44″	97°30′38.52″	Alluvial fan, Gully	I (2)	I (2)	I (2)	I (2)	H (3)	I (11)	9.8 ± 1.1
194.7	49°10′11.11″	97°31′32.26″	Gully	H (3)	I (2)	H (3)	I (2)	H (3)	H (13)	8.4 ± 2.1
196.4	49°10′6.11″	97°32′55.47″	Gully	H (3)	I (2)	I (2)	I (2)	H (3)	I (12)	9.3 ± 1.1
197.6	49°10′1.55″	97°33′51.94″	Gullies	I (2)	H (3)	I (2)	H (3)	H (3)	H (13)	9.8 ± 1.3
198.1	49°9′59.91″	97°34′20.22″	Gullies	H (3)	I (2)	I (2)	I (2)	H (3)	I (12)	8.5 ± 1.1
199.4	49°9′55.86″	97°35′25.80″	Alluvial fan, Gully	I (2)	I (2)	I (2)	I (2)	H (3)	I (11)	8.0 ± 1.3
200.7	49°9′51.94″	97°36′25.22″	Gully	H (3)	I (2)	I (2)	H (3)	H (3)	H (13)	7.9 ± 1.4
201.2	49°9′49.47″	97°36′51.82″	Alluvial fan, Gully	H (3)	I (2)	I (2)	I (2)	H (3)	I (12)	8.2 ± 0.8
202.2	49°9′47.31″	97°37′53.45″	Alluvial fan, Gully	I (2)	H (3)	I (2)	I (2)	H (3)	I (12)	7.4 ± 0.5
203	49°9′46.36″	97°38′19.36″	Alluvial fan, Gully	I (2)	I (2)	I (2)	I (2)	H (3)	I (11)	6.1 ± 1.0
203.5	49°9′45.00″	97°38′44.12″	Alluvial fan, Gully	H (3)	I (2)	I (2)	I (2)	H (3)	I (12)	6.3 ± 1.5
203.7	49°9′44.58″	97°38′54.18″	Stream, Riser	H (3)	H (3)	I (2)	H (3)	H (3)	H (14)	5.1 ± 0.8
204	49°9′43.71″	97°39′7.75″	Gully	H (3)	I (2)	I (2)	I (2)	H (3)	I (12)	4.3 ± 0.6
204.2	49°9′43.09″	97°39′19.45″	Gullies	I (2)	I (2)	H (3)	I (2)	H (3)	I (12)	4.9 ± 1.2
204.4	49°9′41.94″	97°39′29.88″	Gully	I (2)	H (3)	H (3)	H (3)	H (3)	H (14)	5.0 ± 0.9
204.9	49°9′40.50″	97°39′51.64″	Gully	H (3)	H (3)	L (1)	H (3)	H (3)	H (13)	4.4 ± 0.6
205.3	49°9′39.78″	97°40′11.05″	Mountain Ridge	I (2)	I (2)	H (3)	I (2)	H (3)	I (12)	5.0 ± 0.9

Table 1 *(continued)*

Locality			Geomorphic offset marker							
				Data quality[b]						
No.[a]	Latitude	Longitude	Type	OMW	OMS	RZW	PZW	IQ	Summation	Horizontal Offset (m)
205.8	49°9′39.11″	97°40′34.88″	Gullies	H (3)	I (2)	H (3)	H (3)	H (3)	H (14)	4.6 ± 1.0
207.7	49°9′36.54″	97°42′9.02″	Stream	H (3)	H (3)	I (2)	I (2)	H (3)	H (13)	3.3 ± 0.7
207.9	49°9′36.89″	97°42′20.24″	Stream	I (2)	I (2)	I (2)	I (2)	H (3)	I (11)	3.6 ± 1.1
Bulnay rupture (section-H)										
214.1	49°9′36.61″	97°47′17.90″	Stream, Riser	I (2)	H (3)	I (2)	H (3)	H (3)	H (13)	7.5 ± 1.5
215.6	49°9′32.21″	97°48′33.55″	Stream, Riser	I (2)	I (2)	I (2)	I (2)	H (3)	I (11)	8.5 ± 1.1
217.3	49°9′28.23″	97°49′56.62″	Gully	I (2)	I (2)	I (2)	I (2)	H (3)	I (11)	8.2 ± 0.5
218.8	49°9′24.55″	97°51′10.50″	Stream	I (2)	I (2)	H (3)	H (3)	H (3)	H (13)	8.6 ± 0.7
220.5 (s)	49°9′35.23″	97°52′32.25″	Stream, Riser	H (3)	I (2)	H (3)	I (2)	H (3)	H (13)	2.6 ± 0.6
222	49°9′24.81″	97°53′45.63″	Gullies	L (1)	L (1)	I (2)	L (1)	H (3)	L (8)	8.2 ± 1.2
224.9	49°9′20.33″	97°56′10.78″	Gully	I (2)	L (1)	I (2)	L (1)	H (3)	L (9)	8.5 ± 1.7
227.3	49°9′16.67″	97°58′8.25″	Stream, Riser	H (3)	H (3)	I (2)	H (3)	H (3)	H (14)	7.5 ± 0.8
228.5	49°9′13.00″	97°59′14.97″	Stream, Riser	I (2)	I (2)	H (3)	I (2)	H (3)	I (12)	8.8 ± 1.1
229.7	49°9′11.83″	98°0′9.86″	Alluvial fan, Gully	I (2)	H (3)	I (2)	I (2)	H (3)	I (12)	8.6 ± 2.0
233.2	49°9′7.94″	98°3′1.85″	Stream, Riser	I (2)	I (2)	I (2)	I (2)	I (2)	I (10)	8.1 ± 1.5
234.4	49°9′2.25″	98°3′57.53″	Stream	I (2)	I (2)	I (2)	I (2)	I (2)	I (10)	8.8 ± 1.6
237.1	49°8′52.53″	98°7′51.20″	Stream	L (1)	L (1)	L (1)	L (1)	L (1)	L (5)	9.3 ± 1.0
240.8	49°8′48.57″	98°9′12.35″	Gully	I (2)	I (2)	I (2)	I (2)	I (2)	I (10)	9.8 ± 1.3
241.7	49°8′48.30″	98°9′56.54″	Stream Riser	L (1)	L (1)	L (1)	L (1)	L (1)	L (5)	9.8 ± 1.6
243.9	49°8′42.92″	98°11′48.64″	Stream, Riser	I (2)	I (2)	I (2)	I (2)	I (2)	I (10)	10.3 ± 0.6
245.7	49°8′39.28″	98°13′15.93″	Stream	I (2)	I (2)	I (2)	I (2)	I (2)	I (10)	9.3 ± 1.2
252.6	49°8′56.48″	98°18′55.28″	Stream Riser	I (2)	I (2)	I (2)	I (2)	I (2)	I (10)	8.9 ± 1.7
258.5	49°8′45.88″	98°23′46.55″	Stream	I (2)	I (2)	I (2)	I (2)	I (2)	I (10)	5.4 ± 1.1
Bulnay rupture (section-I)										
264.3	49°9′1.95″	98°28′38.04″	Stream	I (2)	I (2)	I (2)	I (2)	I (2)	I (10)	4.9 ± 1.2
271.9	49°8′49.05″	98°34′48.73″	Gully	L (1)	I (2)	L (1)	L (1)	L (1)	L (6)	6.2 ± 1.3
273.1	49°8′46.58″	98°35′46.61″	Gully	I (2)	I (2)	I (2)	I (2)	I (2)	I (10)	5.6 ± 0.9
274.5	49°8′48.09″	98°36′58.17″	Gully	I (2)	I (2)	I (2)	I (2)	I (2)	I (10)	6.6 ± 0.5
277.3	49°8′43.58″	98°38′24.00″	Gully, Riser	I (2)	I (2)	I (2)	I (2)	I (2)	I (10)	6.8 ± 1.5
278.5	49°8′43.17″	98°39′24.27″	Gully, Riser	I (2)	I (2)	I (2)	I (2)	I (2)	I (10)	6.3 ± 1.0
279	49°8′43.46″	98°39′50.06″	Gully, Riser	I (2)	I (2)	I (2)	I (2)	I (2)	I (10)	6.4 ± 2.3
281.9	49°8′35.91″	98°42′10.33″	Gully, Riser	I (2)	I (2)	I (2)	I (2)	I (2)	I (10)	5.3 ± 0.6
283.8	49°8′32.74″	98°43′45.22″	Gully	L (1)	I (2)	L (1)	I (2)	L (1)	L (7)	5.0 ± 0.9
288	49°8′16.92″	98°48′3.39″	Gully, Riser	I (2)	I (2)	I (2)	I (2)	I (2)	I (10)	5.1 ± 1.4
289.7	49°8′15.21″	98°48′35.74″	Gully, Riser	I (2)	I (2)	I (2)	I (2)	I (2)	I (10)	5.5 ± 1.6
Bulnay rupture (eastern end section)										
294.6	49°8′21.26″	98°52′34.00″	Gully	L (1)	L (1)	L (1)	L (1)	L (1)	L (5)	4.8 ± 1.0
297.4	49°8′22.99″	98°55′1.94″	Gully	L (1)	L (1)	L (1)	I (2)	L (1)	L (6)	3.5 ± 0.9
304.2	49°8′42.75″	99°0′29.40″	Gully	L (1)	I (2)	I (2)	L (1)	L (1)	L (7)	3.5 ± 0.5
309.3	49°9′15.10″	99°4′36.55″	Gully	L (1)	L (1)	L (1)	L (1)	L (1)	L (5)	2.7 ± 0.4
Teregtiyn rupture (northwestern section)										
13.3	49°16′52.00″	94°57′3.34″	Gully	H (3)	H (3)	H (3)	I (2)	H (3)	H (14)	1.7 ± 0.5
Teregtiyn rupture (southeastern section)										
17.3	49°15′37.27″	94°59′44.67″	Stream, Riser	H (3)	I (2)	I (2)	I (2)	H (3)	I (12)	3.0 ± 0.8
18.78	49°15′5.08″	95°0′38.65″	Streams	I (2)	I (2)	I (2)	I (2)	H (3)	I (11)	2.2 ± 0.6
18.81	49°15′5.08″	95°0′38.65″	Streams	I (2)	I (2)	I (2)	I (2)	H (3)	I (11)	2.0 ± 0.1
21.5	49°13′59.36″	95°2′10.63″	Stream, Riser	H (3)	I (2)	I (2)	H (3)	H (3)	H (13)	2.6 ± 0.2
23.7	49°13′4.06″	95°3′19.64″	Gully	I (2)	I (2)	H (3)	I (2)	H (3)	I (12)	3.4 ± 0.7
24.1	49°12′52.48″	95°3′33.41″	Gully	I (2)	H (3)	H (3)	H (3)	H (3)	H (14)	3.0 ± 0.5
25	49°12′29.98″	95°4′1.02″	Stream, Riser	I (2)	I (2)	H (3)	I (2)	H (3)	I (12)	3.5 ± 1.0
26	49°12′8.26″	95°4′31.52″	Gully	I (2)	L (1)	H (3)	I (2)	H (3)	I (11)	3.4 ± 0.4
26.2	49°12′2.77″	95°4′39.84″	Gully, Riser	H (3)	I (2)	H (3)	I (2)	H (3)	H (13)	3.4 ± 0.8
27	49°11′43.32″	95°5′8.26″	Stream, Riser	I (2)	I (2)	I (2)	H (3)	H (3)	I (12)	4.2 ± 1.0
28	49°11′20.78″	95°5′38.46″	Gully	H (3)	I (2)	H (3)	I (2)	H (3)	H (13)	3.9 ± 1.0
28.6	49°11′5.11″	95°5′58.60″	Alluvial fan, Gully	H (3)	I (2)	I (2)	I (2)	H (3)	I (12)	3.8 ± 0.9
37.4	49°6′55.00″	95°9′37.47″	Alluvial fan, Gully	H (3)	I (2)	H (3)	I (2)	H (3)	H (13)	3.3 ± 0.7
38	49°6′41.56″	95°9′54.41″	Gully	H (3)	I (2)	I (2)	I (2)	H (3)	I (12)	3.1 ± 0.8

Table 1 *(continued)*

Locality			Geomorphic offset marker							
				Data quality[b]						
No.[a]	Latitude	Longitude	Type	OMW	OMS	RZW	PZW	IQ	Summation	Horizontal Offset (m)
38.2	49°6′35.48″	95°10′1.64″	Gully	H (3)	I (2)	I (2)	I (2)	H (3)	I (12)	4.0 ± 0.9
42.8	49°4′26.92″	95°11′54.86″	Alluvial fan, Gully	I (2)	H (3)	H (3)	H (3)	H (3)	H (14)	3.9 ± 0.5
49.3	49°1′18.43″	95°14′14.18″	Gully	H (3)	H (3)	H (3)	I (2)	H (3)	H (14)	2.9 ± 0.7
50.5 (s)	49°0′37.97″	95°14′28.52″	Stream	H (3)	I (2)	H (3)	H (3)	H (3)	H (14)	1.2 ± 0.3
62.7	48°54′32.53″	95°18′6.60″	Gully, Riser	H (3)	I (2)	I (2)	I (2)	H (3)	I (12)	3.0 ± 0.3
63.4	48°54′11.31″	95°18′19.62″	Gully	H (3)	I (2)	H (3)	H (3)	H (3)	H (14)	2.2 ± 0.5

[a]Each locality no. is marked by distance (km) from the epicenter along the fault in the direction of rupture propagation and (−) for the opposite direction. (s) indicates that an offset was measured on a secondary rupture strand. [b]In order to assess data quality, for each offset five criteria were evaluated: OMW = Offset Marker Width; OMS = Offset Marker Straightness; RZW = Rupture Zone Width; PZW = Plausible Zone Width; IQ = Image Quality. A score is attributed for each criterion: 3 points for high (H), 2 points for intermediate (I), and 1 point for low (L) (see Figure S1 for details). The final assessment of data quality based on the total score is 15–13 points for high, 12–10 points for intermediate, and less than 10 points for low.

represents cumulative deformation. We have considered that offset variation could be unrealistic when the slip varies by more than 50% between adjacent sites along the same rupture section. Eventually, it appears that the majority of discarded data are larger than the maximum 1905 coseismic offset and are similar to the second smallest offsets estimated at adjacent multiple-offset sites. As a result, we have produced a first sub–data set of 276 offset measurements that we confidently associate with the 1905 coseismic horizontal slip distribution (Figure 4 and Table 1). The subsequent part of this study will focus only on the 1905 sub–data set analyses.

To complement our image analysis, we carried out two field campaigns in July 2014 and July 2015. During field reconnaissance, special attention was given to locations with complex geometry. We visited about 30 offset features along five different sections of the rupture to check the consistency of our satellite-based mapping and offset measurements against field observation. No major discrepancy was found, and, on average, field measurements and satellite measurements are consistent (see examples in Figures 3b–3d). Because HRS image analysis is intrinsically limited to detection of the horizontal deformation, we also visited locations where we suspected existence of some additional dip-slip component, to quantify both the horizontal and vertical components of deformation. Such dip-slip component is mostly limited to fault stepping or bending zones.

4. Mapping Results: The 1905 Rupture Geometry and Slip Distribution

The following section provides an overview of our mapping results for individual rupture sections, which are delimited by abrupt changes of rupture geometry and/or slip distribution. To simplify the discussion, each studied site is referred to by the abbreviation of the fault name and its distance from the epicenter, increasing in the direction of propagation of the rupture (Figure 4a). For example, in Figure 2a, "Bul-E-62 km" indicates the site at 62 km east of the epicenter along the Bulnay fault. Locations of epicenters for the Tsetserleg and the Bulnay earthquakes are, respectively, (N49°31′; E97°22′) and (N49°20′; E94°51′), following Schlupp and Cisternas (2007).

4.1. Surface Rupture Along the Tsetserleg Fault

The epicentral location and source modeling of the Tsetserleg earthquake (Schlupp & Cisternas, 2007) show that the rupture was initiated on a central section and propagated bilaterally (Figure 4a). This central section is about 47 km long and is predominantly located in mountainous terrain. The average azimuth is 62°. The surface rupture is dominantly left-lateral slip, as demonstrated by the orientation of tension cracks and mole tracks visible where the rupture goes across alluvial piedmonts (Figure S2a). In the mountain range, the rupture zone is wider with numerous secondary ruptures and cracks whose location and orientation are likely controlled by inherited structures associated to local foliated volcanic rocks formation (Figure S2b). Although Khil'ko et al. (1985) described continuous south facing reverse scarps along this section, it is not apparent on the HRS images. We measured the 1905 coseismic offsets at 19 sites along the main rupture, which yield an

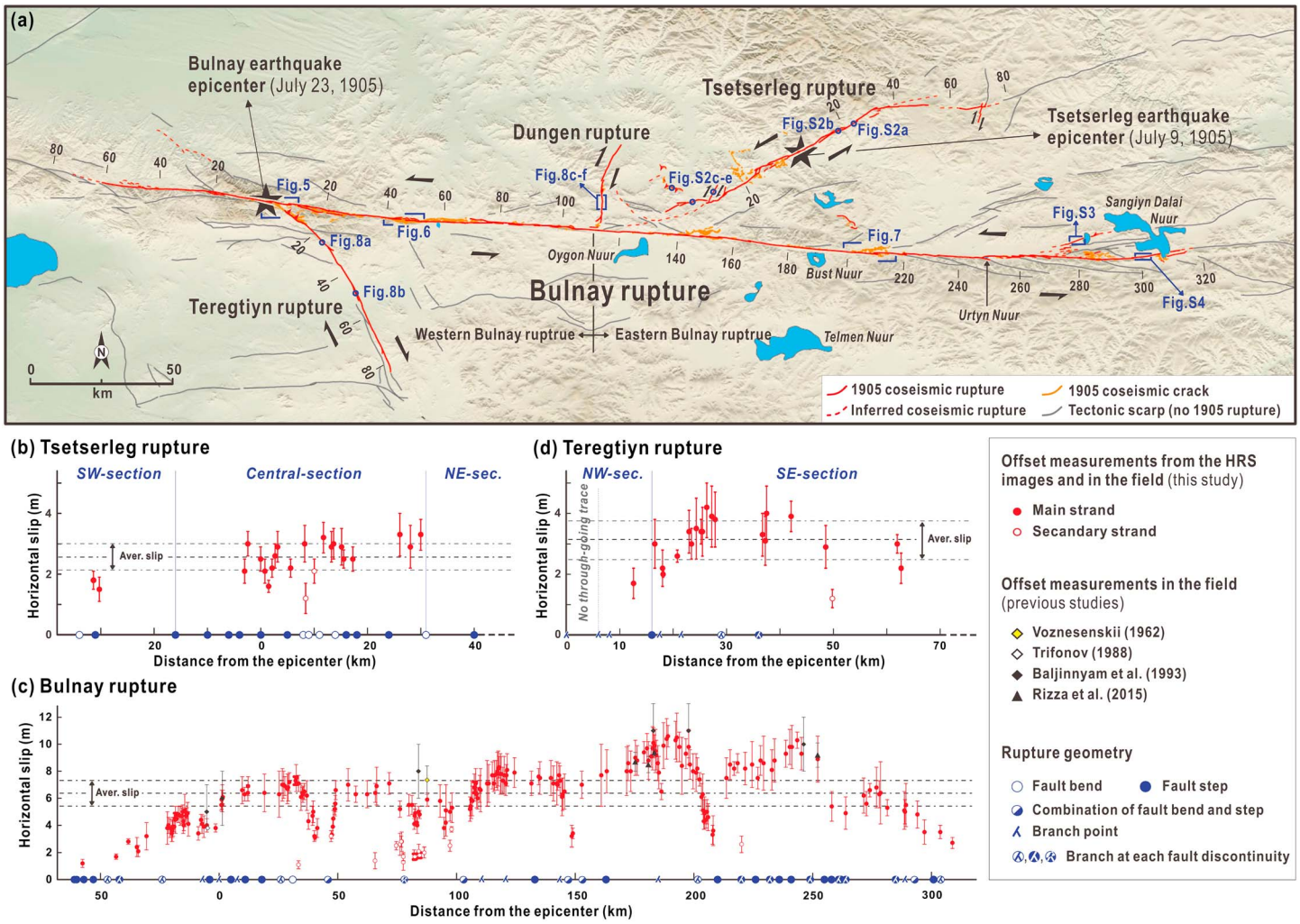

Figure 4. (a) Map of the 1905 Tsetserleg-Bulnay earthquakes surface rupture. Main rupture strands are in red. Secondary deformation is in orange. Dashed line shows extent of inferred surface breaks on the high-resolution satellite images. Stars show epicenter locations for each event after Schlupp and Cisternas (2007). Distances (km) from the epicenters are marked along each major rupture. (b–d) Distributions of horizontal slip along each major rupture. Data are listed in Table 1. Major variability is usually related to complex rupture patterns, such as fault bends, steps, and branches (see text for discussion).

average offset of 2.67 ± 0.43 m. In addition, two offsets larger than 1 m were measured along secondary ruptures (Figure 4b).

At "Tse-NE-31 km," the Tsetserleg rupture bends clockwise ~30° and it extents for a distance of 32 km in a nearly E-W direction (Figure 4a). Further to the east, the surface rupture returns to an ENE-SWS strike for an additional 13 km. To the east-northeast, from "Tse-NE-76 km," although we could follow continuous tectonic scarps for a distance of at least 60 km, we could not find evidence for surface deformation unambiguously associated with the 1905 Tsetserleg earthquake. Eventually, close to the northeastern end of the Tsetserleg rupture, we mapped a 7 km long conjugate rupture, involving right-lateral slip, which is oriented NNE-SSW (Figure 4a). Along the Tsetserleg rupture between Tse-NE-31 km and its northeastern end, we could not measure any displacement associated to 1905 due to the absence of markers.

At "Tse-SW-16 km," the main rupture jumps through a 1.6 km wide releasing step (Figure 4a). To the northwest from the fault step, numerous cracks are distributed over a long distance (up to about 10 km). Mostly, they follow topographic contours, suggesting that they could be, in part, gravity driven. Further southwestward, for a distance of 22 km from the fault step, the rupture shows typical features of left-lateral slip. Offsets were measured at two locations, which yield an average slip of 1.65 ± 0.35 m (Figure 4b). Vivid surface breaks along the main stretch of the Tsetserleg fault vanished near "Tse-SW-38 km," where they

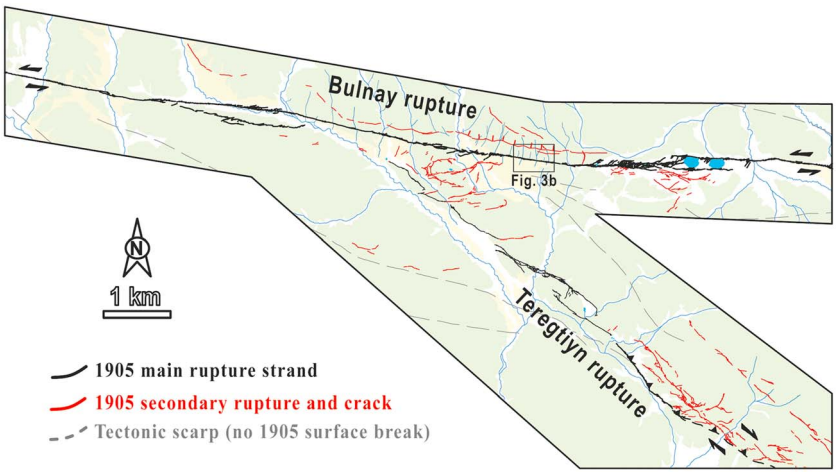

Figure 5. Map of the 1905 coseismic surface rupture around the epicenter of the Bulnay earthquake. Highly distributed deformation is highlighted by dense cracking at junction between conjugated Bulnay and Teregtiyn faults.

splay into three different kind of secondary faults (Figures S2c–S2e): (1) nearly E-W trending left-lateral faults; (2) NNE-SSW trending right-lateral faults, which are similar to the one documented at the northeastern end of the Tsetserleg rupture; and (3) WNW-ESE trending thrust faults. These secondary ruptures, for a total distance of 29 km, are partly located along lithological boundaries of Paleozoic felsic volcanic rocks with granitic rocks or Quaternary sediments. At the southwestern end of the Tsetserleg rupture Khil'ko et al. (1985) reported tectonic scarps as 1905 coseismic ruptures (see the dashed line in Figure 4a). However, we could not find unambiguous evidence supporting that interpretation.

4.2. Surface Rupture on the Bulnay Fault

The 388 km long surface rupture along the Bulnay fault can be divided into western and eastern sections. The boundary between the two parts is located near "Bul-E-110 km," close to the intersection between the Bulnay fault and the Dungen fault (Figure 4a). These two sections are characterized by differences in rupture complexity and amount of coseismic offset. In the following sections we describe characteristics of the ground rupture and coseismic offsets for the different sites along the Bulnay rupture. We pay special attention to local variation in the amount of offset and its relations to variations in rupture geometries.

4.2.1. Around the Epicenter Area

The Bulnay earthquake initiated near the junction between the Bulnay fault and the Teregtiyn fault (Figure 4). In the epicentral area along the Bulnay fault, the rupture pattern can be described as (1) the main strike-slip rupture running at the base of the mountain front, (2) few continuous secondary ruptures subparallel to the main strands located north of the main rupture, and (3) a densely fractured area on the southern side of the main rupture (Figure 5). The main rupture, showing an azimuth of 100°, is localized along a single strand characterized by a series of tension cracks displaying right-stepping en echelon geometry. Some of these cracks currently have a sigmoidal shape suggesting that they formed during some previous earthquake and were later sheared by one or several subsequent ruptures, including the 1905 event. We interpreted those as evidence of cumulative deformation. In this fault section, we measured left-lateral offsets at five sites, which yield an average slip of 5.80 ± 0.62 m (Figure 4c).

North of the main rupture strand, vertical counterslope scarps were formed with a maximum normal throw of 0.5 m down to the north and are roughly parallel to the main rupture (Figure 5). No cumulative deformation is observed on this secondary faulting. The northward dip of these normal faults suggests that they do not connect with the main fault at depth, as in a classic slip-partitioning case (King et al., 2005) but are rather guided by local preexisting geologic structures. On the southern side of the main rupture, cracks with a wide range of lengths and orientations are distributed between the Bulnay and Teregtiyn faults (Figure 5). Along these, we could not find clear evidence for horizontal slip. Hence, we interpret these cracks to result from local extension in the inner corner of the junction between two conjugate faults, the Bulnay fault and the Teregtiyn fault.

4.2.2. From the Epicenter to the Western End of the Surface Rupture

From the epicenter westward, the rupture is mainly characterized by a 100° trending linear strand (Figure 4a). Because the rupture crosses small gullies and river terraces, we can observe geomorphic offsets of high quality on the HRS images. These indicate nearly pure left-lateral slip. The 1905 coseismic slip was measured at 27 sites (Figure 4c), and it averages 4.22 ± 0.65 m. At "Bul-W-24 km," the rupture shows a 10° anticlockwise azimuth change to the west, with damage affecting the inner part of the bend. West of this bend, the fault is characterized by a single strand for 23 km, and we were able to measure coseismic offsets at five sites, yielding an average offset of 2.44 ± 0.50 m (Figure 4c). Further west, at "Bul-W-47 km," the coseismic rupture bends back clockwise by about 10° to 100° and continues westward for 16 more kilometers. Only one coseismic offset has been measured along that section, which is 1.20 ± 0.30 m (Figure 4c).

Assessing the exact western end point of the 1905 rupture remains difficult. Khil'ko et al. (1985) suggested that the end of the 1905 coseismic surface rupture was located about 75 km west of the epicenter. However, on the HRS images, westward from "Bul-W-63 km" it is difficult to identify a rupture that can be unambiguously attributed to the 1905 event, although the continuation of the fault trace is clearly visible. In fact, we measured ~20 horizontal offsets along the further 25 km long scarp to the west, but most of these offsets exceed 10 m, with no evidence for smaller recent individual offset. Hence, we suggest that these offsets are cumulative offsets related to older earthquakes rather than offsets due to the 1905 event. In addition, Bul-W-63 km marks a transition in the local geology with the fault cutting through massive intrusive rocks and a change of fault azimuth (gradually clockwise about 10°) in regional scale caused by the fault entering zone of transpressional deformation (Figure 1c). These changes, with the observation that on the HRS images we could not find any offsets consistent with what was measured further east, suggest that the 1905 rupture stopped very close to Bul-W-63 km (Figure 4).

4.2.3. From the Epicenter to "Bul-E-103 km"

From the epicentral area to "Bul-E-26 km," an azimuth of the Bulnay rupture is 98°. Running parallel to the main rupture, about 1 km to the south, there is a continuous secondary rupture, fresh enough that it is likely associated to the 1905 event. However, because the area is forested, it was not possible to determine with certainty the style of deformation along this secondary strand, or to measure any offset, from the HRS images. From the strike of this rupture, which has a 5° of difference with the main fault, however, we infer that it is likely left-lateral faulting with some thrust component. The area between the main and secondary ruptures is heavily cracked (Data Set S1). We measured coseismic offsets at six sites along the main strand (Figure 4c) that yield an average offset of 6.48 ± 0.98 m.

Between Bul-E-26 km and "Bul-E-31 km" the rupture rotates ~7° anticlockwise to be nearly E-W, before resuming an azimuth of 97° for the next 10 km eastward. Along this section, between Bul-E-26 km and "Bul-E-41 km," the rupture is mostly a single strand, providing high-quality offset markers. We measured a relatively constant coseismic slip, with an average of 6.93 ± 0.95 m, at six sites within the western first 5 km. In contrast, at 16 sites along the next 10 km, slip is gradually decreasing from the maximum of 7.5 ± 1.0 m in the west, to the minimum of 3.1 ± 0.2 m in the east (Figure 4c). Such decrease in slip is attributed to the existence of the large-scale fault bend that starts around Bul-E-41 km.

Between Bul-E-41 km and "Bul-E-50 km" the Bulnay rupture bends gradually anticlockwise about 6°, producing local compression in the inner part of the bend (Figure 6). The rupture splays into two strands, each one accommodating one specific component of the deformation, following a classic slip-partitioning scheme (Eberhart-Phillips et al., 2003; King et al., 2005; Toda et al., 2016). The range-front strand shows dominant strike-slip movement, while the secondary strand, dominated by thrust faulting, has propagated northward through the alluvial fans that slope down from the range-front. The geometric relation between the two strands, which is low-angle dipping thrust fault less than 1 km apart from vertical strike-slip fault, suggests that the thrust strand likely joins the main fault strand at a depth of 1 to 2 km. Because the strike-slip strand is discontinuous in places, with numerous small fault steps and branches, it is difficult to accurately measure offsets. Only in the eastern part where the geometry is simpler that we are able to measure a series of eight offsets related to 1905 faulting. These measurements increase eastward from 3.2 ± 0.4 m to 6.6 ± 0.7 m (Figures 4c and 6b), as the restraining bend progressively ends. The secondary strand shows typical features of thrust fault scarps, such as a highly sinuous rupture trace and dense cracks on the hanging-wall (Figure 6). GPS-derived topography along 10 profiles across the thrust strand reveals that it is a composite scarp with break in slopes and a steeper front. We estimate an average 1.37 m of vertical offset associated with the

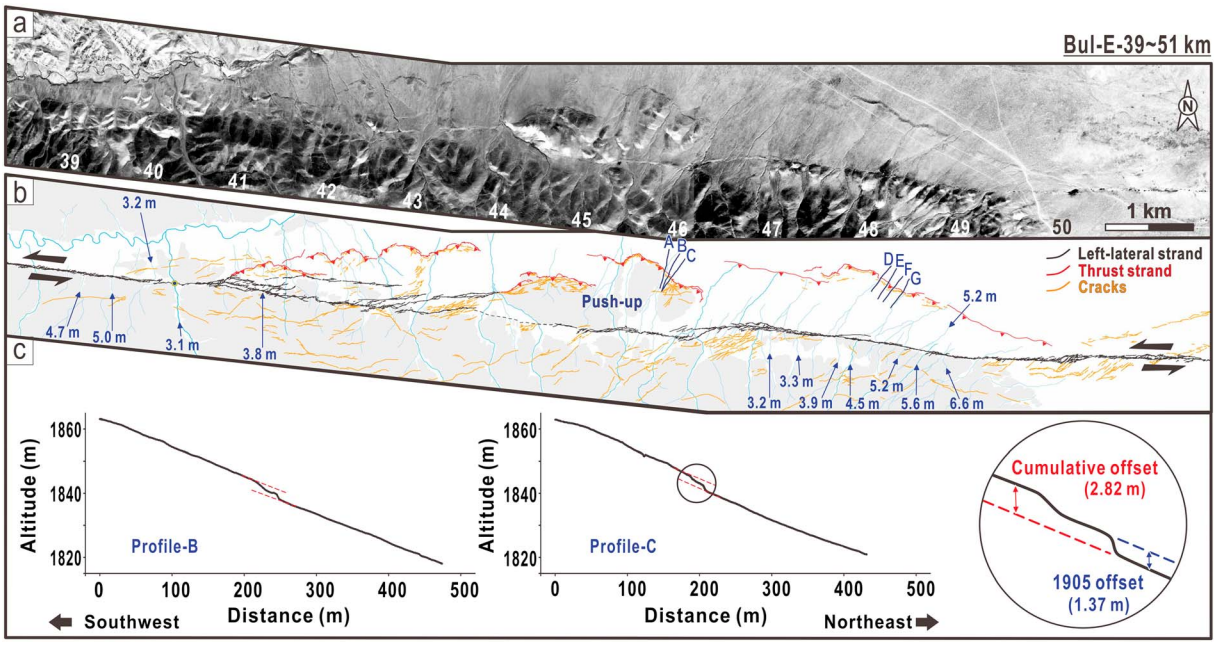

Figure 6. (a, b) High-resolution satellite mapping for the 1905 coseismic surface breaks associated with change of fault azimuth near "Bul-E-46 km." The compressional geometry results in partitioning of the deformation between a strike-slip strand and a thrust strand. Cumulative displacements on both rupture traces suggest that it is a perennial behavior. Intense cracking south of the strike-slip fault is associated to propagation-related off-fault damage (see discussion in text). (c) Two examples of kinematic Global Positioning System vertical profiles (A–G) across the thrust rupture. Inset highlights that the scarp is cumulative.

1905 rupture and 2.82 m of cumulative offset (Figure 6c). Numerous cracks were mapped next to the two main splays of the rupture: Fault-parallel cracks are located in the hanging-wall of the thrust scarps, probably associated with breaking of the neck of the thrust during the rupture. Tension cracks, showing about 28° of angular relation with the strike-slip strand, are also widely distributed in the mountain range south of the strike-slip strand. These cracks show asymmetric spatial distribution with cracks only on the southern side of the eastward propagating left-lateral rupture. Hence, we suggest that these cracks correspond to a typical signature of off-fault coseismic damage associated with the outer part of the bend.

At Bul-E-50 km, the two ruptures merge into a single linear strand showing an azimuth of 91°. This section continues for 28 km through a flat basin, until "Bul-E-78 km," and is characterized by a succession of tension cracks and mole tracks, with the width of the deformation zone varying between 10 m and few tens of meters (Figure 2a). Although the wide rupture zone hampers accurate measurements of coseismic slip, an average slip of 6.46 ± 0.90 m was estimated from seven offset markers on the HRS images (Figure 4c). Numerous secondary ruptures were detected north of the main strand, at a distance of up to 1.5 km, although it is difficult to determine their actual style of deformation due to the small amount of displacement detected on the HRS imagery.

At Bul-E-78 km, the azimuth of the rupture bends clockwise about 6° to 97°. For 25 km eastward, the 1905 coseismic rupture consists mostly of two parallel strands (Figures 2d and 2e). On average, the two strands are about 200 m apart. The southern strand has a reverse slip component in addition to the dominant left-lateral movement. Dense cracks are mappable within the zone between the two main ruptures. We measured the coseismic horizontal offsets at 16 sites along the northern strand, yielding an average offset of 4.86 ± 0.74 m (Figure 4c). Along the southern strand, we estimated a smaller average slip of 2.23 ± 0.33 m from seven sites. The total horizontal offset across the two strands is about 7 ± 1 m. This is consistent with previous studies that, respectively, reported coseismic left-lateral offsets of 6.3 m–8.2 m (Voznesenskii, 1962) and 8 ± 2 m (Baljinnyam et al., 1993) along the same fault section. It is difficult to directly compare our measurements with their results, however, because they did not describe the multiple rupture strands (Figure 4c).

4.2.4. From Bul-E-103 km to "Bul-E-249 km"

Between Bul-E-103 km and "Bul-E-144 km," the main rupture mainly runs along the southern front of the mountain range (Figure 4a). The rupture strand shows an azimuth of 92° and passes in close proximity of

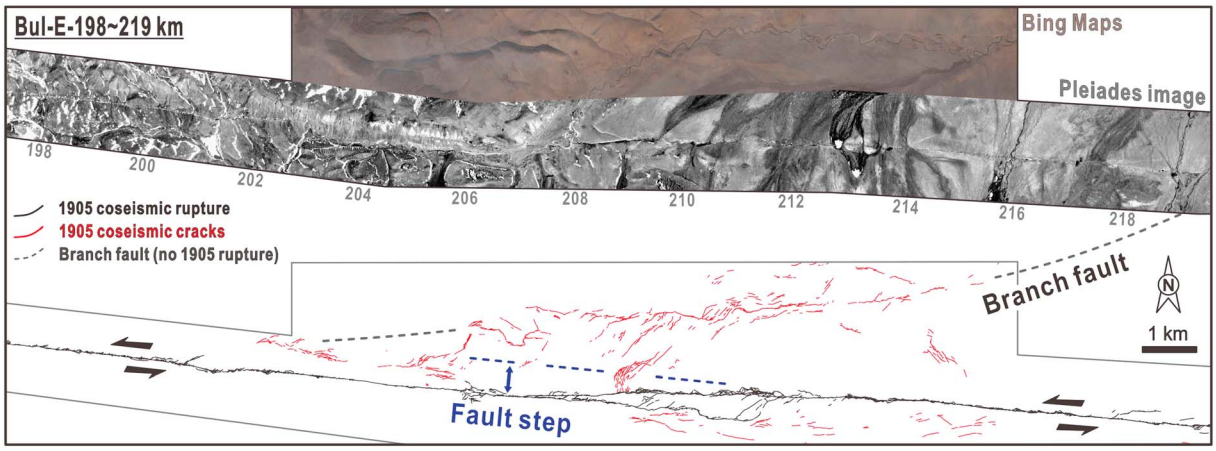

Figure 7. The 1905 coseismic surface rupture for a distance of ~20 km around "Bul-E-210 km." This section is characterized by existences of a fault step as well as one major branch fault, which was not activated during the 1905 T-B EQs, on the northern side of the Bulnay fault. Secondary cracks are asymmetrically concentrated north of the main fault and are highly distributed along the branch fault.

the Tsetserleg rupture and Dungen rupture. In contrast to the rupture sections described to the west, here the coseismic deformation is highly localized. Secondary faulting remains very limited around the main rupture when it goes through alluvial fans or minor fault steps. The mountain front provides high-quality piercing points for offset markers, and we were able to measure coseismic slip at 37 sites (Figure 4c). They yield an average horizontal slip of 7.16 ± 1.08 m.

From Bul-E-144 km eastward, for a distance of 12 km, the main rupture gradually bends southeast by 6°. This section is characterized by a large number of secondary cracks. North of the rupture, in particular, the cracking is extensive and it affects the entire area between the main rupture and an ENE-WSW branching fault that was not ruptured in 1905 (Figure 4a). We measured coseismic offsets at six sites along the main rupture once one has passed the junction area of the branch fault, from west to east: (1) an average slip of 6.30 ± 1.30 m at three sites, representing about 1 m to 2 m of decrease in slip compared to slip values observed west of the junction area; (2) two smaller offsets: 3.20 ± 0.80 and 3.40 ± 0.40 m, in and around a minor fault step located at the central part of the junction area; and (3) one offset of 7.00 ± 1.00 m on the single-strand trace (Figure 4c). Therefore, the apparent slip deficit observed along this section, which can be as large as about 50% of total slip, is most likely due to distribution of slip onto parallel secondary faulting and dense cracking.

Between Bul-E-156 km and "Bul-E-202 km," the rupture strand shows an azimuth of 98° on average (Figure 4 a). Along this section, the width of the rupture zone is usually narrower than 10 m. We have measured coseismic offsets at 32 sites, yielding an average horizontal slip of 9.00 ± 1.30 m, in good agreement with what was already documented along this section (Baljinnyam et al., 1993; Rizza et al., 2015; Figure 4c). At Bul-E-181 km, however, the offset value drops locally by about 3 m relative to the average value, as the rupture passes through the close proximity of a secondary fault nonruptured in 1905 that branches northeastward (Figures 4a and 4c). From Bul-E-202 km eastward, the rupture pattern becomes more complex, again with many secondary ruptures and cracks, as another fault is branching northeastward (Figures 4a and 7). The 1905 coseismic rupture occurred along both the main and branch faults. In the latter cases, however, only the first ~10 km of the branch was ruptured, starting from the branching point. Here the main rupture is characterized by a local azimuth change of 6° for a few kilometers that corresponds to accommodation of a 530 m wide fault step. On the main strand, we recognized a steady eastward decrease of coseismic offset, from 7.4 ± 0.5 m to 3.3 ± 0.7 m, at 12 sites between Bul-E-202 km and "Bul-E-210 km," which we attribute to distribution of slip between the main rupture and the branch (Figure 4c). Although we could not recognize it on HRS images, Baljinnyam et al. (1993) reported 1 to 2 m of normal slip along the secondary branches.

From Bul-E-210 km eastward, the rupture shows an average azimuth of 92° for a distance of 39 km. Along this section the rupture pattern is simple with a series of linear strands, about 5 to 10 km long, connected by fault steps, such as the Urtyn Nuur Lake, which corresponds to a 780 m wide pull-apart. Horizontal offsets, measured mainly on central parts of each section, range from 7.50 ± 1.50 m to 10.3 ± 0.6 m. It yields an

average value of 8.74 ± 1.21 m for 16 sites (Figure 4c). Near a fault step at "Bul-E-220 km," we measured a small offset of 2.6 ± 0.6 m along one of the secondary ruptures.

4.2.5. From Bul-E-249 km to the Eastern End of the Surface Rupture

For 15 km east of the lake "Urtyn Nuur" the Bulnay fault is characterized by a succession of short sections connected by steps, either compressional or extensional. Unfortunately, this section is partially covered with forest and available HRS images are of poor quality, resulting in only limited possibilities for offset measurement. We measured two coseismic offsets: 8.9 ± 1.7 m and 5.4 ± 1.1 m, within this section. The largest one was previously recognized by Rizza et al. (2015), who obtained a similar offset value (Figure 4c).

Along the next 29 km eastward from the "Bul-E-264 km," the Bulnay rupture extends through volcanic mountain ranges with an average azimuth of 93°. In addition to the main rupture, numerous surface breaks were found north of the main trace (Figure 4a). Especially, starting at "Bul-E-261 km," systematic northeastward splay faults branch off the main rupture. The longest branch is at least 23 km long, where it enters the lake "Sangiyn Dalai Nuur" (Figure S3). Other splay faults are only 5 to 7 km long. We measured coseismic offsets at 11 sites along the main rupture strand. They yield an average slip of 5.79 ± 1.20 m, indicating a decrease of slip in comparison with the western rupture sections (Figure 4c).

From Bul-E-293 km eastward, the rupture gradually bends northward and eventually with an azimuth of 75° near the southern edge of the lake Sangiyn Dalai Nuur (Figure 4a). Indeed, this is the most remarkable change of fault azimuth along the entire Bulnay rupture. We measured coseismic offsets at four sites. They indicate a gradual decrease of slip eastward from 4.8 ± 1.0 m to 2.7 ± 0.4 m (Figure 4c). Arzhannikova et al. (2015) reported horizontal offsets ranging from 6.5 to 7.5 m with no or a little vertical component within this section. This would correspond to significant increase of the coseismic slip close to the end of the rupture. Alternatively, we suggest that the larger values could correspond to cumulative deformation that includes 1905 and prior events (Figure S4).

On the southeast side of the lake Sangiyn Dalai Nuur, we observed a ~6 km long secondary rupture parallel to the Bulnay fault, located about 1.5 km away to the south, as well as arrays of few-tens-of-meters-long cracks around the lakeshore (Figure 4a). Although it is difficult to determine the very end point of the 1905 coseismic surface rupture because fault scarps continue farther east along the Bulnay fault, we could recognize a clear surface rupture up to about 4 km to the east from the eastern shoreline of the lake Sangiyn Dalai Nuur. Florensov and Solonenko (1963) similarly reported that the eastern end of the 1905 Bulnay rupture lies just east of the lake.

4.3. Surface Rupture on the Teregtiyn Rupture Zone

The rupture associated with the Bulnay earthquake also propagated to the southeast along the Teregtiyn fault. Following the direction of rupture propagation, we describe the main characteristics of each section from northwest to southeast, starting at km 6 as the very beginning of the Teregtiyn rupture (Figure 5). For a distance of 10 km, the main rupture runs along the southwestern front of mountain ranges with a slightly sinuous strand showing an average azimuth of 125°. The main strand involves both right-lateral and reverse slip components along a northeast dipping fault (Baljinnyam et al., 1993; Khil'ko et al., 1985). Dense arrays of cracks are distributed within a 1 km wide zone on the northeastern mountainside (Figure 5). On HRS images we could measure only one coseismic horizontal offset: 1.7 ± 0.5 m, on the main strand.

Further southeastward at "Ter-SE-16 km," for a distance of 13 km, the rupture is a single linear stand with an azimuth of 138° (Figure 4a). Along that section, the rupture is highly localized and it shows evidence for nearly pure right-lateral slip during the 1905 rupture and in previous events (Figures 8a and 8b). We measured coseismic offsets from 1905 at 12 sites. The offsets generally increase to the southeast, and the average offset is 3.20 ± 0.67 m (Figure 4d). The rupture strand bends ~12° clockwise at "Ter-SE-29 km" and comes out of the mountain range at "Ter-SE-43 km." In this section, we could document coseismic offsets at four sites, with an averaged value of 3.58 ± 0.73 m (Figure 4d).

From Ter-SE-43 km to the southeast, the Teregtiyn rupture crosses a flat basin, striking 152° on average for a distance of about 37 km (Figure 8b). In general, the rupture displays a typical pattern of strike-slip faulting with a linear trace and local variations in the sense of dip-slip (Baljinnyam et al., 1993). The rupture strand occasionally follows the edge of a series of low fault-parallel hills and fault-bounded lakes, which seem to be long-lived pressure ridges and pull-apart basins along the Teregtiyn fault (Data Set S1). Although the

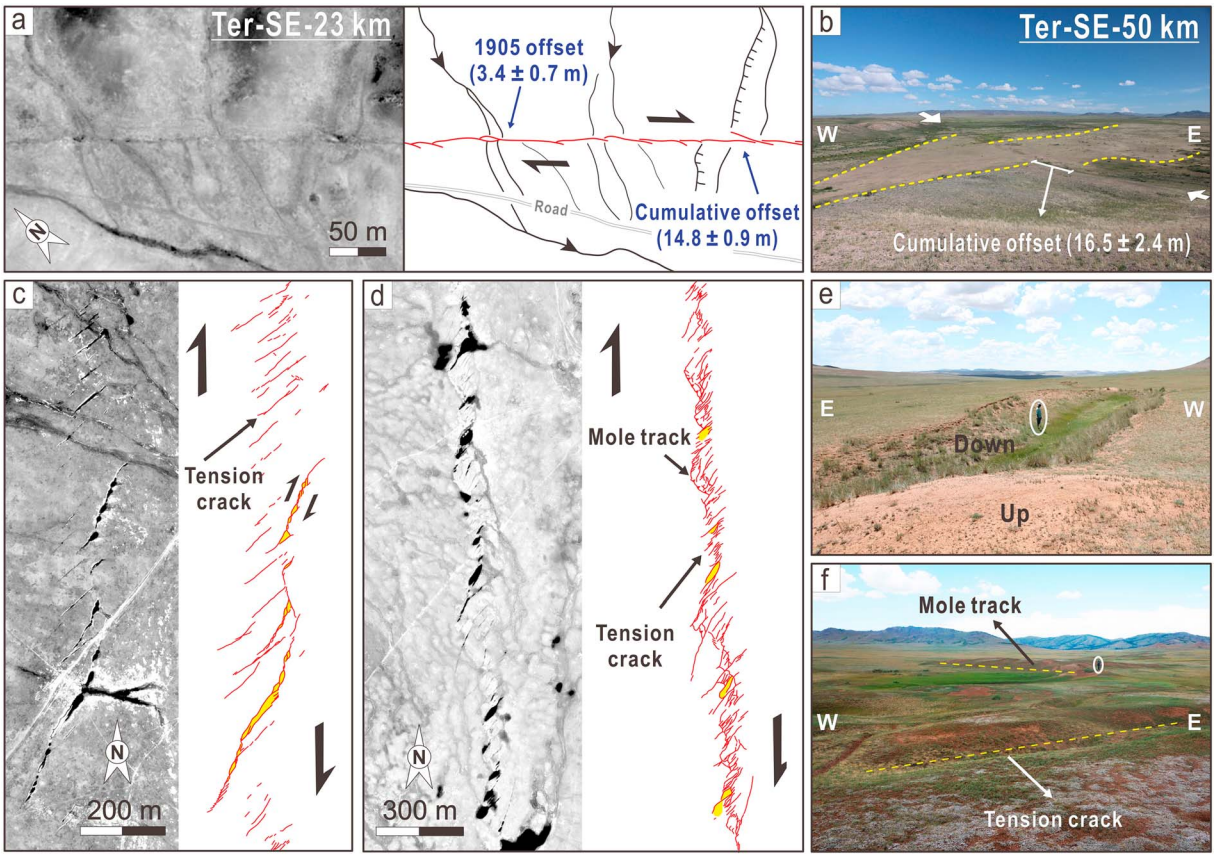

Figure 8. (a) High-resolution satellite mapping including both 1905 coseismic and cumulative offset measurements along the Teregtiyn rupture. (b) Cumulative lateral offset estimated by displaced river risers along the Teregtiyn fault. (c, d) High-resolution satellite mapping along the Dungen rupture. This rupture is mainly characterized by large en echelon tension cracks alternating with mole tracks. (e, f) Field photos showing a series of tension cracks and mole tracks along the Dungen rupture. People for scale.

1905 rupture strand is somewhat more complex around the pressure ridges, the primary deformation seems to be localized within a narrow rupture zone without notable fault steps and bends. On the HRS images, we measured coseismic horizontal offsets, ranging from 2.2 ± 0.5 to 3.0 ± 0.3 m, at three sites along the main strand (Figure 4d). For the secondary strands, we could find only one offset marker indicating a right-lateral component of 1.2 ± 0.3 m. At "Ter-SE-80 km," where the Teregtiyn rupture is believed to end (Baljinnyam et al., 1993; Khil'ko et al., 1985), it remains difficult to determine with certainty if observed fault scarps are associated with the 1905 earthquake or with older events. It is worth noting that we could observe offsets larger than 5 m at a limited number of sites near "Ter-SE-70 km" in the field, and we interpret these offsets as cumulative deformation that includes the 1905 event.

4.4. Surface Rupture on the Dungen Fault

The Dungen fault, which is located to the northern side of the central part of the Bulnay rupture (Figure 4a), also ruptured in 1905. The Dungen fault connects with the Bulnay rupture at a right angle. The junction also corresponds to the location where the projection of the Tsetserleg rupture would have intersected the Bulnay rupture. Based on the HRS images and field reconnaissance, we could trace the Dungen rupture for a distance of 35 km (Figure 4a), about 10 km longer than previous recognized (Baljinnyam et al., 1993). Overall, the rupture zone is composed of a series of en echelon tension cracks, often in combination with a series of mole tracks, with no visible throughgoing rupture along its entire length (Figures 8c and 8d). The left stepping arrangement of the tension cracks indicates right-lateral slip of the Dungen rupture. Each crack is generally characterized by dimensions of tens of meters in length and a few meters in width (Figures 8e and 8f). In some cases, individual cracks have tension cracks at their tips and this implies that they involve a right-lateral shear as well as an extensional component (Figure 8c). There is no measurable offset due to the wide and

complex rupture zone. Baljinnyam et al. (1993) inferred 1–2 m of horizontal slip on average based on the dimensions of tension cracks.

Our mapping suggests that the Dungen rupture consists of two distinct sections displaying slightly different fault strikes and deformation intensity (Figure 4a). To the south, the nearly N-S trending Dungen rupture consists of relatively large tension cracks. Some of these cracks are longer than 100 m and are connected by mole tracks perpendicular to them. To the north, the rupture bends clockwise ~20° and it becomes simpler with a series of smaller en echelon tension cracks. Thus, the overall geometry of the Dungen rupture suggests that the amount of surface deformation is higher to the south, where it approaches to the Bulnay rupture. Indeed, the Dungen rupture does not fully connect to the Bulnay rupture. Close to junction, the Dungen rupture splits into two strands that extend southward only for a short distance (about 2.5 km) to end about 3 km north of the Bulnay fault. On the HRS images, tension cracks are distributed across a 1 km wide zone at the very end of one of these branches.

5. Discussion

The 676 km long surface rupture associated with the 1905 T-B EQs exhibits various degrees of geometric complexity depending on location along the fault. Some of this complexity could be attributed to permafrost at the time of the rupture (Baljinnyam et al., 1993), but rupture complexity and off-fault damage are most likely related to fundamental processes such as interaction between preexisting structural fault complexities or local lithological variability and the propagating rupture. The impact of such processes was already partially recognized for some other strike-slip events of similar size (Bhat et al., 2007; Haeussler et al., 2004; Klinger et al., 2005; Vallage et al., 2015, 2016). In the next sections, we take advantage of the detailed rupture map, along with a dense slip distribution, to explore different characteristics of the rupture pattern to see how they inform us on the control of rupture during a large strike-slip event.

5.1. Effects of Segment Geometry on Rupture Propagation

Strike-slip faults are classically described as segmented, with segments having a direct impact on the rupture processes (King & Nabelek, 1985; Wesnousky, 2006). However, recognizing individual segment boundaries is not always easy. Some boundaries are characterized by clear geometric changes in the fault, mapping into steps either extensional or compressional. Some boundaries, however, are more difficult to detect as they relate to small changes in fault azimuth, or interaction with side faults. Therefore, it is only when an earthquake occurs that such segmentation becomes obvious (Klinger, 2010). Although it is unlikely to see two significant seismic ruptures along the same fault section that would allow comparing rupture patterns, it appears, based on geomorphological observations, that fault segmentation is not necessarily evolving significantly during each earthquake. Hence, segmentation lasts for several seismic cycles, which is long enough to leave some recognizable imprint in the landscape.

The 1905 T-B EQs surface rupture, as described in previous sections, is distributed on four main faults: the Tsetserleg fault, the Teregtiyn fault, the Dungen fault, and the Bulnay fault (Figure 4). Using detailed mapping, we have been able to characterize the diversity of geometrical discontinuities along the Bulnay rupture (Figure 9a and Table 2). These discontinuities are of two types: fault steps and fault azimuth changes. Although steps have been recognized as potential segment boundaries (Wesnousky, 2006, 2008), the role of fault azimuth changes has been less considered, so far. In the case of the Bulnay rupture, it appears that many segments are actually defined by fault bends. These bends are on average about 6.6° and, in some cases, they extend laterally over several kilometers. In most cases, bends are coincident with local slip decrease (Figures 9a and 9b). Large-scale steps, which can be several hundred meters wide (up to 780 m along the Bulnay rupture), are also collocated with fault bends. Conversely, smaller-size steps less than 200 m wide are not systematically associated with fault bends and they impact less significantly the slip distribution, although their size still indicates that they are perennial structures lasting several earthquake cycles. Interestingly, both ends of the Bulnay rupture are actually characterized by significant fault bends, which are not associated with major steps.

Following Klinger (2010), based on geometrical discontinuities, including fault azimuth changes, and slip variations, we have identified 4, 2, 2, and 11 to 13 individual geometric segments for the ruptures of Tsetserleg, Teregtiyn, Dungen, and Bulnay faults, respectively (Figure 9b and Table 3). Using offset

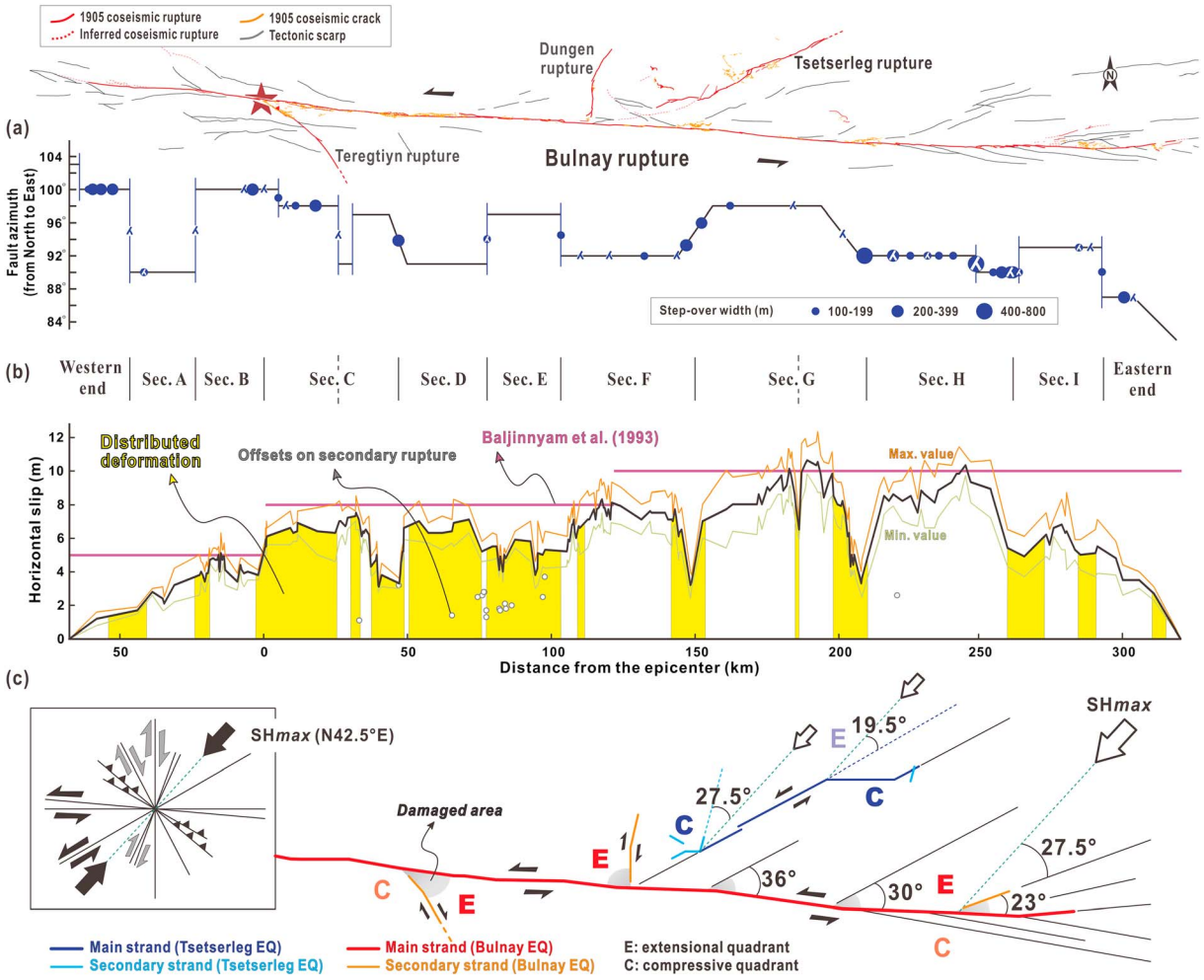

Figure 9. Fault segmentation of the 1905 Bulnay rupture, assessed based on fault discontinuities and along-fault slip variations. (a) Geometrical features are highlighted by changes of fault azimuth as well as locations of fault steps (circle) and branch points (junction). In some cases, fault azimuth changes appear to occur gradually over a distance of several kilometers and different kinds of fault discontinuities can be colocated. In the cases of fault steps, the symbol size scales with step over width. (b) Slip distribution including Max. and Min. values along the main rupture strand. The fluctuating slip distribution indicates that the Bulnay rupture consists of 11, possibly up to 13, major rupture sections that are defined mainly by changes of fault azimuth. Previously suggested slip distribution is marked for comparison. Zones of intensively distributed deformation around the main rupture are indicated in yellow. They correlate with slip decreases along the main rupture both at local and full-rupture scales (see text for discussion). (c) Simplified map of the 1905 Tsetserleg-Bulnay earthquakes surface rupture showing orientations and sense of slip for major branch faults. Regional stress and main rupture directions are shown for reference. Highly damaged zones near junction points of the branch faults, in gray, are mainly located in extensional quadrants.

measured only across the main rupture strand, average offset for each segment was computed by adding all offsets and then dividing by the number of data. For five segments along the Bulnay rupture, two different average values could be obtained, whether offsets at intersegment zones were included or not in the computation (Table 3). The difference of average slip between adjacent segments is ~1.3 m (Table 3). On average the length of each segment is about 29 km with a standard deviation of 13 km, which is in the upper range of values previously proposed for strike-slip segments in continental settings (Klinger, 2010). We attribute this difference to presence of a thicker seismogenic crust in 1905 T-B EQs region, as suggested by recent geophysical and geodetic results (Calais et al., 2003; Déverchère et al., 2001; Nielsen & Thybo, 2009).

In parallel to fault bending and stepping zones, another typical feature that has been proved to affect earthquake rupture process is branching of the rupture along side faults. If the rupture branches, the rupture often ends up in a cul-de-sac where it stops (Bhat et al., 2004; Klinger et al., 2006, 2017), leaving the main fault unbroken. In many cases, however, rupture branching fails and rupture resumes along the main fault after branching

Table 2
Major Fault Discontinuities Defined on the Basis of Fault Bends (Greater Than 5°) and Fault Steps (Wider Than 100 m) for Individual Major Ruptures Associated With the 1905 T-B EQs

	Fault bend[b]		Fault step			
			Releasing		Restraining	
Locality[a]	Clockwise	Anticlockwise	Length (m)	Width (m)	Length (m)	Width (m)
Tsetserleg rupture (from southwest to northeast)						
SW-34	26°					
SW-31			710	240		
SW-16			850	1,600		
SW-10			760	620		
SW-6			440	210		
SW-4					DB-760[c]	330
0			310	240		
NE-5					DB-280	230
NE-8		19°				
NE-9	11°					
NE-11	15°					
NE-14		13°				
NE-16					DB-710	150
NE-18			540	200		
NE-24			(−)930[d]	270		
NE-31	30°					
NE-40			0	180		
NE-52	12°					
NE-63		20°				
Bulnay rupture (from west to east)						
W-61			120	150		
W-60			−80	240		
W-57			−540	290		
W-53			−300	250		
W-47	10°					
W-42			150	100		
W-24		10°				
W-4			−220	270		
E-5			900	190		
E-11			390	140		
E-18					DB-1520	280
E-26		7°				
E-31	6°					
E-41~50		6°				
E-46			−860	240		
E-78[e]	6°		350	130		
E-103		5°			DB-910	180
E-133			30	120		
E-144~156	6°					
E-149			160	220		
E-156			470	200		
E-163			300	120		
E-194~210		6°				
E-210			350	530		
E-220			370	270		
E-226			680	110		
E-232			−30	180		
E-236			210	190		
E-241			−50	130		
E-249			−1000	780		
E-255			330	160		
E-258					DB-1150	280
E-261			470	390		
E-262			−250	200		
E-264			−230	190		

Table 2 *(continued)*

	Fault bend[b]		Fault step			
			Releasing		Restraining	
Locality[a]	Clockwise	Anticlockwise	Length (m)	Width (m)	Length (m)	Width (m)
E-285					DB-1450	190
E-293		6°	−510	190		
E-301			350	210		
E-304		5°				
Teregtiyn rupture (from northwest to southeast)						
SE-16	13°					
SE-29	12°					
SE-36					DB-1100	450
Dungen rupture (from south to north)						
N-11		10°				
N-19	23°				290	450

Note. See also Figure 9.
[a]Each locality is marked by the direction of rupture propagation and its distance (km) from the epicenter. In the case of the Dungen rupture, the distance is estimated from its junction with the Bulnay fault. [b]The direction of fault bends is based on the rupture propagation direction. [c]"DB" indicates that the fault jog is defined by a double-bends geometry. [d]The attached sign "–" means that the fault step occurs between underlapping fault segments. [e]For fault discontinuities defined by a combination of fault step and bend, each parameter is independently presented.

attempts (Vallage et al., 2016). Indeed, successful rupture branching requires specific configuration of the regional stress direction relative to the azimuth of the main fault and branch (Poliakov et al., 2002). In addition, past-earthquake history of the fault (Schwartz et al., 2012) and rupture velocity (Bhat et al., 2007; Kame et al., 2003) are also parameters to be considered to enhance chances for successful rupture branching.

The 1905 Bulnay earthquake rupture involves branching at two different scales. We can distinguish major branches along two conjugate faults, the Teregtiyn fault and the Dungen fault. We also observe shorter branches, with lengths $\leq$10 km. The Teregtiyn and Dungen branches are characterized by a dominant right-lateral slip, antithetic to the main Bulnay rupture. In both cases, the junction between the branch and the Bulnay rupture is not fully developed and no throughgoing rupture can be observed in the field. Instead, the areas located between the Bulnay rupture and the beginning of the well-localized branch rupture are heavily damaged with numerous discontinuous cracks, still visible at surface (Figure 5). This is particularly true in the wedge-shaped fault block that corresponds to extension for both the main rupture and the branch rupture (Figure 9c). Such lack of direct connection might be due to the fact that the junction area is intrinsically unstable and cannot develop a long-term fault trace signature (Klinger et al., 2017). The impact of these two branches on the slip distribution of the Bulnay rupture is difficult to assess. In the case of the Teregtiyn fault, the epicenter of the 1905 Bulnay event is located at or very near the junction between the two faults (Schlupp & Cisternas, 2007). Hence, west of the junction, along sections A and B, the slip is steadily decreasing to end about 50 km away from the epicenter (Figure 9). East of the junction, along sections C, D, and E, the slip is rather constant with an average value of 6.64 ± 0.82 m. The section east of section E corresponds to the projected intersection with the Dungen fault. It is also where the southwestern part of the Tsetserleg rupture would have connected to the Bulnay fault if it had gone through. East of this section, slip gradually increases as 1.74 ± 0.41 m and reaches an average 8.37 ± 1.22 m horizontal offset along sections F, G, and H as the Bulnay rupture starts to have a simpler geometry with less off-fault damage.

In addition to these two major branches, numerous shorter branches can be found along the main Bulnay rupture, mostly along its eastern section (Figure 4a). They do not exceed 10 km in length and usually do not have significant slip, except toward the eastern end of the rupture where they become more preeminent. Because the azimuth of the Bulnay rupture changes gradually to be more E-W near its eastern end, the angle between the main rupture direction and the regional geological fabric (ENE-WSW trending branch faults) gets smaller, which is more favorable to initiate branching (Figure 9c). Distribution of these branches is uneven with most branches located north of the Bulnay rupture. This is interpreted as resulting from the interaction of the inherited ENE-WSW trending faults with the propagating left-lateral Bulnay rupture from

Table 3
Fault Segmentation of the 1905 T-B EQs Surface Rupture

Rupture section		Length (km) Main strand	Length (km) Secondary strand	Average horizontal offset (m) Including offsets in interseg-ment zones	Average horizontal offset (m) Excluding offsets in interseg-ment zones
Tsetserleg rupture (from southwest to northeast)					
Subsidiary ruptures at	Left-lateral slip		15	—	—
The southwestern end	Right-lateral slip		7	—	—
	Thrust slip		7	—	—
Southwestern section (SW-38 km[a] ~ SW-16 km)		22		1.65 ± 0.35	1.65 ± 0.35
Central section (SW-16 km ~ NE-31 km)		47		2.67 ± 0.45	2.67 ± 0.45
Northeastern section (NE-31 km ~ NE-63 km)		32		—	—
Northeasternmost section (NE-63 km ~ NE-76 km)		13		—	—
Subsidiary rupture at the northeastern end			7	—	—
Total		114	36	2.57 ± 0.44	2.34 ± 0.42[b]
Bulnay rupture (from west to east)					
Western end section (The western end ~ W-47 km)		22[c]		1.20 ± 0.40	1.20 ± 0.40
Section A (W-47 km ~ W-24 km)		23		2.44 ± 0.50	2.44 ± 0.50
Section B (W-24 km ~ Epicenter)		24		4.22 ± 0.65	4.22 ± 0.65
Section C	C1 (Epicenter ~ E-26 km)	46	26	6.04 ± 0.76	6.51 ± 0.80
	C2 (E-26 km ~ E-46 km)		20		
Section D (E-46 km ~ E-78 km)		32		5.68 ± 0.71	6.46 ± 0.90
Section E[d] (E-78 km ~ E-103 km)		25		7.09 ± 0.74	7.09 ± 0.74
Section F (E-103 km ~ E-150 km)		47		6.91 ± 1.07	7.10 ± 1.09
Section G	G1 (E-150 km ~ E-181 km)	60	31	7.89 ± 1.19	9.05 ± 1.32
	G2 (E-181 km ~ E-210 km)		29		
Section H (E-210 km ~ E-261 km)		51		8.56 ± 1.23	8.75 ± 1.24
Major splay rupture (branched out at the E-261 km)			23	-	-
Section I (E-261 km ~ E-293 km)		32		5.79 ± 1.20	5.79 ± 1.20
Eastern end section (E-293 km ~ E-319 km)		26		3.63 ± 0.70	3.63 ± 0.70
Total		388	23	6.31 ± 0.95	6.37 ± 0.95
Teregtiyn rupture (from northwest to southeast)					
Northwestern section	No throughgoing trace	6		—	—
(Epicenter ~ SE-16 km)	Throughgoing trace	10		1.70 ± 0.50	1.70 ± 0.50
Southeastern section (SE-16 km ~ SE-80 km)		64		3.20 ± 0.65	3.20 ± 0.65
Total		80		3.13 ± 0.65	2.90 ± 0.63
Dungen rupture (from south to north)					
Souther section	No throughgoing trace	3		—	—
(Junction point ~ N-19 km)	Throughgoing trace	16		—	—
Norther section (N-19 km ~ N-35 km)		16		—	—
Total		35		—	—
The entire surface rupture		617	59	—	—

[a]Each locality is marked by the direction of rupture propagation and its distance (km) from the epicenter. For the Dungen rupture, the distance is estimated from its junction with the Bulnay fault. [b]When we exclude offset data in intersegment zones, average offsets for each major rupture are calculated by adding multiples of length and average offset for all individual segments and then dividing by the total length of each rupture. [c]The length of the western end section is based on a median value of the inferred rupture lengths. [d]As the rupture in Section E is mainly composed of two-parallel rupture strands, the average slip is estimated by adding average slips on each strand.

west to east and defines the northern side as the extensional side, which is more prone to branching (Poliakov et al., 2002). The fact that none of the branch faults in the extensional side of the eastern Bulnay fault eventually succeeded in developing as a full-scale large rupture suggests that the 1905 Bulnay rupture was probably not propagating with a supershear velocity (Bhat et al., 2007; Kame et al., 2003).

Figure 9b shows the slip distribution along the Bulnay fault, from the 1905 earthquake. This distribution is consistent with slip distribution reported previously (Baljinnyam et al., 1993). However, the major increase

in the number of measurements shows that the previous study favors the largest offset values, which are easier to see in the field. This led to an overestimation of the average slip associated to the 1905 Bulnay event by about 2 m. Although the Bulnay rupture can be segmented into 11 to 13 sections, with most of the boundaries associated with fault bends and/or steps, the slip distribution is rather smooth along the entire rupture. Small localized variations of slip are seen where the fault azimuth changes, which reflect some distribution of the slip on secondary faults that are part of the fault bend. The general pattern, however, shows that the slip does not vary much from one segment to the next, and the only trend that can be seen unambiguously is the increase of slip when moving eastward along the rupture trace, which is discussed further below.

5.2. Asymmetry in Slip Distribution Along the Bulnay Rupture

Along-strike slip distribution for large strike-slip earthquakes can vary significantly. In some cases, it is highly variable with bursts of slip along some sections of the earthquake rupture alternating with sections with more limited slip (Berberian et al., 1999; Klinger et al., 2006; Rockwell & Klinger, 2013). In other examples, the slip distribution along the rupture is relatively smooth with no distinct peaks (Klinger et al., 2011; Lindvall et al., 1989). What makes such difference is not yet well understood. The impact of geometrical asperities on the variability of the slip distribution, however, has long been recognized (Choi et al., 2012; Klinger, 2010; Wesnousky, 2006). The slip distribution of the 1905 T-B EQs is one more example of an earthquake where slip on the main rupture would locally decrease as the rupture propagates across geometric changes (Figure 9), due to distribution of part of the slip on secondary faults associated with fault bends and steps.

More interesting is the general pattern of slip associated to the 1905 T-B EQs. One can distinguish the eastern part from the western part in the slip distribution, which join near "Bul-E-110 km" (Figure 4a). With exception of both ends of the rupture, each part shows a rather constant average slip, with the slip along the western part being about 2 m smaller on average than slip along the eastern part. In parallel, Figure 9b shows the general distribution of secondary faulting along the Bulnay rupture, based on our detailed mapping. Damage, which is represented by secondary ruptures and cracks, is distributed unevenly between the western and the eastern parts. Along the western part, damage is ubiquitous along the main rupture. In most places, one can find parallel ruptures and intense cracking, still visible more than a century after the event. Conversely, along the eastern part, with the exception of few short branches found close to the eastern end, deformation is highly localized along one single trace. Damage is mostly limited to boundaries of adjacent segments. Hence, we suggest that the total slip along the western and eastern parts of the Bulnay rupture is actually very similar and that the difference of slip observed along the main rupture is due to some fraction of the deformation (~21% if we consider average offsets of 8.37 m and 6.64 m for the western and eastern part of the Bulnay rupture) that is accommodated by the secondary deformation. Along section E exhibiting two parallel ruptures (Figures 2d and 2e), we have been able to measure slip of about 2 m along secondary faults (Figure 9b), corresponding to the difference between the average slip along the eastern and western parts of the main rupture strand. Therefore, the difference in slip between the western and eastern parts of the Bulnay rupture does not seem to be related to the occurrence of the Tsetserleg event just prior to the Bulnay event but rather to some differences in the mechanical context of the rupture. Figure 1c shows that the geologic framework between the two parts of the rupture is different. Along the eastern part, the fault has propagated through a rather homogeneous body of Cambrian sedimentary rocks. Along the western part, however, the fault has propagated through a patchwork of geological formations, including intrusive rocks, sedimentary rocks, and metamorphic rocks. Hence, along the western section, in many locations, the rupture propagates along a fault plane separating walls with different lithology. In this context of bimaterial interface the propagating rupture would favor off-fault damage on one side or the other, depending on relative properties (mostly stiffness) of the different materials (Duan, 2008), while propagation in a more homogeneous medium along the eastern part might favor better localization of the rupture.

5.3. Earthquake Moment Magnitude

Among standing questions when one directly measures slip at the surface from offset features is to assess how much slip is actually missing that cannot be measured because it would be distributed off fault. Although several recent studies seem to converge on the fact that potential slip deficit at the surface (Fialko et al., 2005) was more than an artifact due to our inability to correctly assess the full displacement across the rupture zone (Kaneko & Fialko, 2011; Vallage et al., 2015), the question of slip distribution could

Table 4
Calculation of M_o and M_w Based On Our Revised Rupture Parameters

Rupture width (km)[a]	Rupture section	Length (km)	Slip (m)	MO × 1,027 (dyne cm^2)MO × 1,027 (dyne cm^2)	Mw
Tsetserleg earthquake					
10	Tsetserleg rupture	114	2.57	0.879	**7.26**
25				2.197	**7.53**
50				4.395	**7.73**
80				7.032	**7.86**
Bulnay earthquake					
10	Bulnay rupture	388	6.37	7.415	**7.91**
	Teregtiyn rupture	80	3.13	0.751	
25	Bulnay rupture	388	6.37	18.537	**8.17**
	Teregtiyn rupture	80	3.13	1.878	
50	Bulnay rupture	388	6.37	37.073	**8.37**
	Teregtiyn rupture	80	3.13	3.756	
80	Bulnay rupture	388	6.37	59.317	**8.51**
	Teregtiyn rupture	80	3.13	6.01	

[a]Four different rupture widths were considered: shallow crust (10 km), seismogenic zone (25 km), entire crust (50 km), or rupture penetration in the upper mantle (80 km).

be attributed to a very localized zone (Rockwell & Klinger, 2013) or in a more distributed fault zone subsists (Rockwell et al., 2002; Vallage et al., 2015). The 1905 T-B EQs is an example, with a section where the deformation is rather distributed with distributed slip amounting to as much as 2 m and a section where the deformation is highly localized.

In the following section we test how such distribution of the deformation impacts the final magnitude of the event, if computed from surface rupture. From our detailed mapping of the rupture, we can derive two quantities: the length and the average slip for each fault section that ruptured during the 1905 T-B EQs (Table 3). The seismic moment associated with the rupture of the Dungen fault, however, has been excluded from our calculation, as we do not have accurate slip data for this rupture. Even if we would adopt Baljinnyam et al. (1993) and consider 1 m to 2 m of average slip for the Dungen rupture, its contribution would not be significant in the total budget of seismic moment released during the earthquakes sequence. Using the relation $M_W = 2/3 \log M_O$—10.7 (Hanks & Kanamori, 1979), we can compute the magnitude M_W for the two main events of the 1905 sequence. The shear modulus is taken to be 3.0×10^{11} for average crustal rocks. Although the rupture thickness is assumed to be 25 km, we also used three alternative values: rupture of a shallow crust (10 km) (Bayasgalan et al., 2005), rupture of the entire crust (50 km), and the case where the rupture would propagate down through a part of lithosphere (80 km) (Schlupp & Cisternas, 2007).

To calculate the seismic moment of the Tsetserleg earthquake, as the slip distribution is incomplete, we simply used the total length of the main rupture strand and the mean average slip estimated from all offset data (Figure 4b). This yields a magnitude M_W between 7.26 and 7.86, depending on the rupture thickness (Table 4). In the case of the Bulnay earthquake, the magnitude was derived from summation of each seismic moment computed for each individual rupture section, based on our fault segmentation (Figure 9b and Table 3). In addition, for the Bulnay rupture we have excluded slip values measured close or in the intersegment zones when averaging slip for each section. Eventually, the average slip combined with the rupture length for both the Bulnay and Teregtiyn ruptures yields a magnitude M_W = 7.91–8.51, depending on the rupture thickness, for the Bulnay earthquake (Table 4). Note that even if the inferred 1 m to 2 m slip associated with off-fault damage on the western Bulnay rupture is included, the resulting magnitude M_W = 7.93 to 8.53 is almost the same.

The seismic moment of the 1905 T-B EQs deduced from the body wave inversion gives a magnitude M_W 8 for the Tsetserleg event and various magnitudes between M_W 8.3 and 8.5 for the Bulnay event (Schlupp & Cisternas, 2007). Because we have already discarded the possibility of significant slip deficit, a possibility to get agreement between the seismological magnitude and our geological magnitude is to consider an unusually wide rupture of 50 km or more for the Bulnay rupture, following Schlupp and Cisternas (2007), who have proposed a depth of 43 km. Although we have no ways to test that hypothesis further, it has been suggested that it could be possible for exceptionally large events (Jiang & Lapusta, 2016). Regional

seismological data, however, do not strongly support such assumption as most earthquakes have a centroid depth around 15 km in the Mongolian region and <10 km in the north of the Hangay dome (Adiya, 2016; Bayasgalan et al., 2005), advocating for normal thickness of the seismogenic crust. Alternatively, we cannot rule out some bias in wave modeling due to very limited data coming almost from similar azimuth and/or miscalibration of the signal.

For the Tsetserleg earthquake, the magnitude derived from surface observations is significantly smaller than the magnitude derived from seismological observations. Rupture depth or rheological parameters could be altered to compensate for the difference in moment estimate, although there are no obvious reasons that they should be different from what was used successfully for the Bulnay calculation. Alternatively, the missing moment could be attributed to some dip-slip component of the Tsetserleg earthquake rupture, as the first-motion fault plane solutions (Molnar & Deng, 1984; Okal, 1977; Figure 1b) and previous field description (Khil'ko et al., 1985) suggested. Or perhaps, as Schlupp and Cisternas (2007) suggested, the Tsetserleg rupture might have been longer than the mapped fault strand. Unlike Schlupp and Cisternas (2007), however, the rupture might also have propagated along part of the fault between the southwestern end of the Tsetserleg rupture and the Bulnay fault (see the dashed line in Figures 1c and 4a). If this part of the rupture would be included in our calculation, although it is not possible to map a throughgoing rupture, we would obtain a magnitude M_W closer or even similar to the magnitude estimated by Schlupp and Cisternas (2007). Hence, we suggest that along its southern termination the Tsetserleg rupture likely did not reach the surface, although it propagated a longer distance than what it indicated by surface rupture solely.

6. Conclusions

Detailed mapping of the 1905 T-B EQs rupture based on the HRS imagery provides us with a revised set of parameters for the coseismic ruptures. The average horizontal slip and rupture length are, respectively, 2.34 ± 0.42 m over at least 114 km for the Tsetserleg rupture, 6.37 ± 0.95 m over ~388 km for the Bulnay rupture, and 2.90 ± 0.63 m over ~80 km for the Teregtiyn rupture. For the main Bulnay rupture, more specifically, we obtain comprehensive slip distribution, geometric segmentation, and the type and size of steps and bends associated with the segment geometry. This leads us to estimate the moment magnitude for the major fault segments. Our results show that beyond local apparent complexity, the surface rupture associated with the sequence is consistent at the rupture scale. Actually, we could demonstrate that location of off-fault branching, mostly along the northern side of the rupture, is directly related to the direction of rupture propagation, enhanced by some structural imprints in the regional geological units. Along the Bulnay rupture, off-fault damage related to rupture propagation is mostly found along the western part of the rupture, while the eastern part of the rupture is more localized. Accordingly, the average slip along the western part of the rupture is smaller by ~2 m compared to average slip along the eastern part. It is found, however, that where it is possible to measure slip on secondary deformation, such as along the western part of the rupture, the slip reaches 1 to 2 m, which added to the slip on the main rupture matches average slip along the eastern part of the rupture. Talking this into account, the slip distribution is rather even along the entire rupture. Because the difference in slip along the main rupture is associated with the difference in off-fault damage, we suggest that any affect of the 9 July Tsetserleg rupture on the variability of the Bulnay slip distribution is minor. Instead, we suggest that local variability in the geological units along the western part of the rupture strongly favors bimaterial behavior, which enhances off-fault damage, and consequently impacts the slip distribution. Hence, although detailed geologic mapping of areas affected by large earthquakes is not always available, our results show that it proves to be a useful addition for understanding earthquake rupture patterns. Unlike variation of frictional properties or stress heterogeneities on the fault plane, geological information is more directly observable and it should be more systematically incorporated into earthquake source process analyses.

Acknowledgments
This work is funded by Research in Paris 2014, GeoSMEC contract ANR-12-BS06–0016, and a grant 2017-MPSS31-006-01030000-2017 from Supporting Technology Development Program For Disaster Management funded by Korean Ministry of Public Safety and Security(MPSS). Images were provided by the French space agency CNES through the Pleaides satellite qualification program. We thank I. Maffat and C. Klinger for their contribution to this work. We thank D. P. Schwartz, E. Nissen, and P. Tregoning for their constructive reviews that greatly improved the manuscript. Supporting information to this article can be found online at https://doi.org/10.6084/m9.figshare.5809272.

References

Adiya, M. (2016). Seismic activity near Ulaanbaatar: Implication for seismic hazard assessment. PhD Thesis. Université de Strasbourg.
Aprodov, V. A. (1960). Seismotectonic observations in the region of the north Hangay earthquake of 1905 (MPR). In *Questions of seismotectonics of pre-Baikal and adjacent territories*: *Bulletin of Soviet Seismology*, *Akademi Nauk USSR* (Vol. 10, pp. 90–97).
Arzhannikova, A. V., Vassallo, R., Arzhannikov, S. G., & Jolivet, M. (2015). Morphotectonis and paleoseismology of the eastern end of the Bulnay fault (Mongolia). *Russian Geology and Geophysics*, *56*, 1484–1490.

Badarch, G., Cunningham, W. D., & Windley, B. F. (2002). A new terrane subdivision for Mongolia: Implications for the Phanerozoic crustal growth of Central Asia. *Journal of Asian Earth Sciences*, *21*, 87–110.

Baljinnyam, I., Bayasgalan, A., Borisov, B. A., Cisternas, A., Demyanovich, M. G., Ganbaatar, L., … Vashchilov, Y. Y. (1993). Ruptures of major earthquakes and active deformation in Mongolia and its surroundings. *Geological Society of America Memoirs*, *181*, 43–52.

Bayasgalan, A., Jackson, J., & McKenzie, D. (2005). Lithosphere rheology and active tectonics in Mongolia: Relations between earthquake source parameters, gravity and GPS measurements. *Geophysical Journal International*, *163*, 1151–1179. https://doi.org/10.1111/j.1365-246X.2005.02764.x

Berberian, M., Jackson, J. A., Qorashi, M., Khatib, M. M., Priestley, K., Talebian, M., & Ghafuri-Ashtiani, M. (1999). The 1997 May 10 Zirkuh (Qa'enat) earthquake (Mw 7.2): Faulting along the Sistan suture zone of eastern Iran. *Geophysical Journal International*, *136*, 671–694.

Bhat, H. S., Dmowska, R., Rice, J. R., & Kame, N. (2004). Dynamic slip transfer from the Denali to Totschunda Faults, Alaska: Testing theory for fault branching. *Bulletin of the Seismological Society of America*, *94*(6B), S202–S213.

Bhat, H. S., Olives, M., Dmowska, R., & Rice, J. R. (2007). Role of fault branches in earthquake rupture dynamics. *Journal of Geophysical Research*, *112*, B11309. https://doi.org/10.1029/2007JB005027

Calais, E., Vergnolle, M., Sankov, V., Lukhnev, A., Miroshnitchenko, A., Amarjargal, S., & Deverchere, J. (2003). GPS measurements of crustal deformation in the Baikal-Mongolia area (1994–2002): Implications for current kinematics of Asia. *Journal of Geophysical Research*, *108*, B102501. https://doi.org/10.1029/2002JB002373

Chery, J., Carretier, S., & Ritz, J.-F. (2001). Postseismic stress transfer explains time clustering of large earthquakes in Mongolia. *Earth and Planetary Science Letters*, *194*(1), 277–286.

Choi, J.-H., Jin, K., Enkhbayar, D., Davvasambuu, B., Bayasgalan, A., & Kim, Y.-S. (2012). Rupture propagation inferred from damage patterns, slip distribution, and segmentation of the 1957 M_W 8.1 Gobi-Altay earthquake rupture along the Bogd fault, Mongolia. *Journal of Geophysical Research*, *117*, B12401. https://doi.org/10.1029/2011JB008676

Déverchère, J., Petit, C., Gileva, N., Radziminovitch, N., Melnikova, V., & San'kov, V. (2001). Depth distribution of earthquakes in the Baikal rift system and its implications for the rheology of the lithosphere. *Geophysical Journal International*, *146*, 714–730.

Duan, B. (2008). Asymmetric off-fault damage generated by bilateral ruptures along a bimaterial interface. *Geophysical Research Letters*, *35*, L14306. https://doi.org/10.1029/2008GL034797

Duan, B., & Oglesby, D. D. (2006). Heterogeneous fault stresses from previous earthquakes and the effects on dynamics of parallel strike-slip faults. *Journal of Geophysical Research*, *111*, B05309. https://doi.org/10.1029/2005JB004138

Eberhart-Phillips, D., Haeussler, P. J., Freymueller, J. T., Frankel, A. D., Rubin, C. M., Craw, P., … Wallace, W. K. (2003). The 2002 Denali Fault earthquake, Alaska: A large magnitude, slip-partitioned event. *Science*, *300*, 1113–1118.

Elliott, J. R., Nissen, E. K., England, P. C., Jackson, J. A., Lamb, S., Li, Z., … Parsons, B. (2012). Slip in the 2010–2011 Canterbury earthquakes, New Zealand. *Journal of Geophysical Research*, *117*, B03401. https://doi.org/10.1029/2011JB008868

Fialko, Y., Sandwell, D., Simons, M., & Rosen, P. (2005). Three-dimensional deformation caused by the Bam, Iran, earthquake and the origin of shallow slip deficit. *Nature*, *435*, 295–299.

Finzi, Y., & Langer, S. (2012). Damage in step-overs may enable large cascading earthquakes. *Geophysical Research Letters*, *39*, L16303. https://doi.org/10.1029/2012GL052436

Florensov, N. A., & Solonenko, V. P. (1963). The Gobi-Altai earthquake (in Russian), Moscow, Akademi Nauk USSR (English translation U.S. Department of Commerce, Washington D.C., 424 p., 1965).

Grandin, R., Socquet, A., Binet, R., Klinger, Y., Jacques, E., de Chabalier, J.-B., … Pinzuti, P. (2009). September 2005 Manda Hararo-Dabbahu rifting event, Afar (Ethiopia): Constraints provided by geodetic data. *Journal of Geophysical Research*, *114*, B08404. https://doi.org/10.1029/2008JB005843

Haeussler, P. J., Schwartz, D. P., Dawson, T. E., Stenner, H. D., Lienkaemper, J. J., Sherrod, B., … Personius, S. F. (2004). Surface rupture and slip distribution of the Denali and Totschunda faults in the 3 November 2002 M 7.9 earthquake, Alaska. *Bulletin of the Seismological Society of America*, *94*(6), S23–S52.

Hanks, T. C., & Kanamori, H. (1979). A moment magnitude scale. *Journal of Geophysical Research*, *84*, 2348–2350.

Harris, R., & Day, S. (1999). Dynamic 3D simulations of earthquakes on en echelon faults. *Geophysical Research Letters*, *26*, 2089–2092.

Hu, F., Zhang, Z., & Chen, X. (2016). Investigation of earthquake jump distance for strike-slip step overs based on 3-D dynamic rupture simulations in an elastic half-space. *Journal of Geophysical Research: Solid Earth*, *121*, 994–1006. https://doi.org/10.1002/2015JB012696

Institute of Geology and Mineral Resources of the Mongolian Academy of Sciences (1998). *The Geological Map of Mongolia at a Scale of 1:1,000,000*.

Jiang, J., & Lapusta, N. (2016). Deeper penetration of large earthquakes on seismically quiescent faults. *Science*, *352*(6291), 1293–1297.

Jolivet, M., Ritz, J.-F., Vassallo, R., Larroque, C., Braucher, R., Todbileg, M., … Arzhannikov, S. (2007). Mongolian summits: An uplifted, flat, old but still preserved erosion surface. *Geology*, *35*, 871–874.

Kame, N., Rice, J. R., & Dmowska, R. (2003). Effects of pre-stress state and rupture velocity on dynamic fault branching. *Journal of Geophysical Research*, *108*(B5), 2265. https://doi.org/10.1029/2002JB002189

Kaneko, Y., & Fialko, Y. (2011). Shallow slip deficit due to large strike-slip earthquakes in dynamic rupture simulations with elasto-plastic off-fault response. *Geophysical Journal International*, *186*(3), 1389–1403.

Khil'ko, S. D., Kurushin, R. A., Kochetkov, V. M., Misharina, L. A., Melnikova, V. I., Giiyova, N. A., … Monhoo, D. (1985). Earthquakes and the Bases of the Seismic Zoning of Mongolia. In *The Joint Soviet–Mongolian Scientific Research Geological Expedition*, *Transactions* (Vol. 41, pp. 19–83).

King, G. C., & Nabelek, J. (1985). The role of fault bends in the initiation and termination of earthquake rupture. *Science*, *228*, 984–987. https://doi.org/10.1126/science.228.4702.984

King, G., Klinger, Y., Bowman, D., & Tapponnier, P. (2005). Slip partitioned surface breaks for the 2001 Kokoxili earthquake, China (Mw 7.8). *Bulletin of the Seismological Society of America*, *95*(2), 731–738.

Klinger, Y. (2010). Relation between continental strike-slip earthquake segmentation and thickness of the crust. *Journal of Geophysical Research*, *115*, B07306. https://doi.org/10.1029/2009JB006550

Klinger, Y., Xu, X. W., Tapponnier, P., Van der Woerd, J., Lasserre, C., & King, G. (2005). High-resolution satellite imagery mapping of the surface rupture and slip distribution of the Mw ~ 7.8, 14 November 2001 Kokoxili earthquake, Kunlun fault, northern Tibet, China. *Bulletin of the Seismological Society of America*, *95*(5), 1970–1987.

Klinger, Y., Michel, R., & King, G. C. P. (2006). Evidence for an earthquake barrier model from Mw ~ 7.8 Kokoxili (Tibet) earthquake slip-distribution. *Earth and Planetary Science Letters*, *242*, 354–364.

Klinger, Y., Etchebes, M., Tapponier, P., & Narteau, C. (2011). Characteristic slip for five great earthquakes along the Fuyun Fault in China. *Nature Geoscience*, *4*, 389–392. https://doi.org/10.1038/NGEO1158

Klinger, Y., Choi, J.-H., & Vallage, A. (2017). Fault branching and long-term earthquake rupture scenario for strike-slip earthquakes. In M. Y. Thomas, T. M. Mitchell, & H. S. Bhat (Eds.), *Fault zone dynamic processes: Evolution of fault properties during seismic rupture* (pp. 217–228). Hoboken, NJ, USA: Wiley & Sons, Inc. https://doi.org/10.1002/9781119156895.ch11

Kurushin, R. A., Bayasgalan, A., Olziybat, M., Enhtuvshin, B., Molnar, P., Bayarsayhan, C., … Lin, J. (1997). The surface rupture of the 1957 Gobi-Altay, Mongolia, earthquake. *Special Papers Geological Society of America*, *320*, 6–65.

Lettis, W., Bachhuber, J., Witter, R., Brankman, C., Randolph, C. E., Barka, A., … Kaya, A. (2002). Influence or releasing step-overs on surface rupture and fault segmentation: Examples from the 17 August 1999 Izmit earthquake on the North Anatolia fault, Turkey. *Bulletin of the Seismological Society of America*, *92*(1), 19–42. https://doi.org/10.1785/0120000808

Lindvall, S. C., Rockwell, T. K., & Hudnut, K. W. (1989). Evidence for prehistoric earthquakes on the Superstition Hills fault from offset geomorphic features. *Bulletin of the Seismological Society of America*, *101*, 385–391.

Lozos, J. C., Oglesby, D. D., Duan, B., & Wesnousky, S. G. (2011). The effects of double fault bends on rupture propagation: A geometrical parameter study. *Bulletin of the Seismological Society of America*, *101*, 385–391.

Mignan, A., Danciu, L., & Giardini, D. (2015). Reassessment of the maximum fault rupture length of strike-slip earthquakes and inference on M_{max} in the Anatolian Peninsula, Turkey. *Seismological Research Letters*, *86*(3), 890–900.

Molnar, P., & Deng, Q. (1984). Faulting associated with large earthquakes and the average rate of deformation in central and eastern Asia. *Journal of Geophysical Research*, *89*, 6203–6227.

Molnar, P., & Tapponnier, P. (1975). Cenozoic tectonics of Asia: Effects of a continental collision. *Science*, *189*, 419–426.

Nielsen, C., & Thybo, H. (2009). No Moho uplift below the Baikal Rift Zone: Evidence from a seismic refraction profile across southern Lake Baikal. *Journal of Geophysical Research*, *114*, B08306. https://doi.org/10.1029/2008JB005828

Nissen, E., Walker, R. T., Bayasgalan, A., Carter, A., Fattahi, M., Molor, E., … Xu, S. (2009). The late Quaternary slip-rate of the Har-Us-Nuur Fault (Mongolian Altai) from cosmogenic Be^{10} and luminescence dating. *Earth and Planetary Science Letters*, *286*, 467–478.

Oglesby, D. D., Mai, P. M., Atakan, K., & Pucci, S. (2008). Dynamic models of earthquakes on the North Anatolian fault zone under the Sea of Marmara: Effect of hypocenter location. *Geophysical Research Letters*, *35*, L18302. https://doi.org/10.1029/2008GL035037

Okal, E. A. (1977). The July 9 and 23, 1905, Mongolian earthquakes: A surface wave investigation. *Earth and Planetary Science Letters*, *34*, 326–331.

Poliakov, A. N. B., Dmowska, R., & Rice, J. R. (2002). Dynamic shear rupture interactions with fault bends and off-axis secondary faulting. *Journal of Geophysical Research*, *107*(B11), 2295. https://doi.org/10.1029/2001JB000572

Pollitz, F., Vergnolle, M., & Calais, E. (2003). Fault interaction and stress triggering of twentieth century earthquakes in Mongolia. *Journal of Geophysical Research*, *108*(B10), 2503. https://doi.org/10.1029/2002JB002375

Ritz, J.-F., Brown, E. T., Bourlès, D. L., Philip, H., Schlupp, A., Raisbeck, G. M., … Enkhtuvshin, B. (1995). Slip rates along active faults estimated with cosmic-ray-exposure dates: Application to the Bogd fault, Gobi-Altai, Mongolia. *Geology*, *23*, 1019–1024.

Ritz, J.-F., Vassallo, R., Braucher, R., Brown, E. T., Carretier, S., & Bourlès, D. L. (2006). Using in situ produced ^{10}Be to quantify active tectonics in the Gurvan Bogd mountain range (Gobi-Altay, Mongolia). *Geological Society of America*, *415*, 87–110.

Rizza, M., Ritz, J.-F., Braucher, R., Vassallo, R., Prentice, C., Mahan, S., … Todbileg, M. (2011). Slip rate and the slip magnitude of past earthquakes along the Bogd left-lateral strike-slip fault (Mongolia). *Geophysical Journal International*, *186*, 897–927. https://doi.org/10.1111/j.1365-246X.2011.05075.x

Rizza, M., Ritz, J.-F., Prentice, C., Vassallo, R., Braucher, R., Larroque, C., … ASTER Team (2015). Earthquake geology of the Bulnay fault (Mongolia). *Bulletin of the Seismological Society of America*, *105*(1), 72–93.

Rockwell, K. T., & Klinger, Y. (2013). Surface rupture and slip distribution of the 1940 Imperial Valley earthquake, Imperial fault, Southern California: Implications for rupture segmentation and dynamics. *Bulletin of the Seismological Society of America*, *103*(2A), 629–640. https://doi.org/10.1785/0120120192

Rockwell, T. K., Lindvall, S., Dawson, T., Langridge, R., Lettis, W., & Klinger, Y. (2002). Lateral offsets on surveyed cultural features resulting from the 1999 Izmit and Duzce earthquakes, Turkey. *Bulletin of the Seismological Society of America*, *92*, 79–94.

Schlupp, A., & Cisternas, A. (2007). Source history of the 1905 great Mongolian earthquakes (Tsetserleg, Bulnay). *Geophysical Journal International*, *169*, 1115–1131.

Schwartz, D. P., Hecker, S., Ponti, D., Stenner, H., Lund, W., & Bayasgalan, A. (2009). The July 23, 1905 Bulnay fault, Mongolia, surface rupture. *Seismological Research Letters*, *80*, 357.

Schwartz, D. P., Haeussler, P. J., Seitz, G. G., & Dawson, T. E. (2012). Why the 2002 Denali fault rupture propagated onto the Totschunda fault: Implications for fault branching and seismic hazards. *Journal of Geophysical Research*, *117*, B11304. https://doi.org/10.1029/2011JB008918

Sieh, K., Jones, L., Hauksson, E., Hudnut, K., Eberhart-Phillips, D., Heaton, T., … Zachariasen, J. (1993). Near-field investigations of the Landers earthquake sequence, April to July 1992. *Science*, *260*(5105), 171–176.

Tapponnier, P., & Molnar, P. (1979). Active faulting and Cenozoic tectonics of the Tien Shan, Mongolia, and Baykal regions. *Journal of Geophysical Research*, *84*, 3425–3459.

Thomas, M. Y., Bhat, H. S., & Klinger, Y. (2017). Effect of brittle off-fault damage on earthquake rupture dynamics. In M. Y. Thomas, T. M. Mitchell, & H. S. Bhat (Eds.), *fault zone dynamic processes: Evolution of fault properties during seismic rupture* (pp. 255–280). Hoboken, NJ, USA: John Wiley & Sons, Inc. https://doi.org/10.1002/9781119156895.ch14

Toda, S., Kaneda, H., Okada, S., Ishimura, D., & Mildon, Z. K. (2016). Slip-partitioned surface ruptures for the Mw 7.0 16 April 2016 Kumamoto, Japan, earthquake. *Earth, Planets and Space*, *68*, 188. https://doi.org/10.1186/s40623-016-0560-8

Trifonov, V. G. (1988). Mongolia-An intracontinental region of predominantly recent strike-slip displacement: Active faults (in Russian). In *Neotectonics and contemporary geodynamics of mobile belts* (pp. 239–272). Moscow: Nauka.

Vallage, A., Klinger, Y., Grandin, R., Bhat, H. S., & Pierrot-Deseilligny, M. (2015). Inelastic surface deformation during the 2013 Mw 7.7 Balochistan, Pakistan, earthquake. *Geology*, *43*(12), 1079–1082.

Vallage, A., Klinger, Y., Lacassin, R., Delorme, A., & Pierrot-Deseilligny, M. (2016). Geological structures control on earthquake ruptures: The Mw7.7, 2013, Balochistan earthquake, Pakistan. *Geophysical Research Letters*, *43*, 10155–10163. https://doi.org/10.1002/2016GL070418

Vassallo, R., Ritz, J.-F., Braucher, R., Jolivet, M., Carretier, S., Larroque, C., … Bourlès, D. (2007). Transpressional tectonics and stream terraces of the Gobi-Altay, Mongolia. *Tectonics*, *26*, TC5013. https://doi.org/10.1029/2006TC002081

Voznesenskii, A. V. (1962). Investigations of the region of the Hangay earthquakes of 1905 in northern Mongolia, *Materials from the Department of Physical geographical Society of the URSS*, no.*1*.

Voznesenskii, A. V., & Dorogostaiskii, V. C. (1914). Map of the earthquakes of 9 and 23 July, 1905 (scale1/420 000) SPb.

Walker, R. T., Bayasgalan, A., Carson, R., Hazlett, R., McCarthy, L., Mischler, J., … Tsolmon, G. (2006). Geomorphology and structure of the Jid right-lateral strike-slip fault in the Mongolian Altay mountains. *Journal of Structural Geology*, *28*, 1607–1622.

Walker, R. T., Molor, E., Fox, M., & Bayasgalan, A. (2008). Active tectonics of an apparently aseismic region: distributed active strike-slip faulting in the Hangay Mountains of central Mongolia. *Geophysical Journal International*, *174*, 1121–1137.

Wesnousky, S. G. (2006). Predicting the endpoints of earthquake ruptures. *Nature*, *444*(7117), 358–360. https://doi.org/10.1038/nature05275

Wesnousky, S. G. (2008). Displacement and geometrical characteristics of earthquake surface ruptures: Issues and implications for seismic-hazard analysis and the process of earthquake rupture. *Bulletin Geological Society of America*, *98*, 1609–1632.

Xu, X. W., Yu, G. H., Klinger, Y., Tapponnier, P., & Van der Woerd, J. (2006). Reevaluation of surface rupture parameters and faulting segmentation of the 2001 Kunlunshan earthquake (Mw 7.8), northern Tibetan Plateau, China. *Journal of Geophysical Research*, *111*, B05316. https://doi.org/10.1029/2004JB003488

Zielke, O., Klinger, Y., & Arrowsmith, J. R. (2015). Fault slip and earthquake recurrence along strike-slip faults: Contributions of high-resolution geomorphic data. *Tectonophysics*, *638*, 43–62.

Zonenshein, L. (1973). The evolution of central Asiatic geosynclines through sea-floor spreading. *Tectonophysics*, *19*, 213–232.